CHAPTER 14

FEMTOSECOND PHOTOPROCESSES: ADSORBATE INFRARED SPECTRAL RESPONSE FOLLOWING VISIBLE PULSE METAL SUBSTRATE EXCITATION

J. P. Culver*, M. Li†, L. G. Jahn*,†, R. M. Hochstrasser†, and A. G. Yodh*

*Department of Physics, †Department of Chemistry,
and the Laboratory for Research on the Structure of Matter
University of Pennsylvania, Philadelphia, PA 19104, USA

Contents

1. Introduction

Femtosecond optical excitation of surfaces creates a unique environment for molecular adsorbates that can initiate surface chemistry.[1] Recent experiments along these lines have shown, for example, that nonequilibrium substrate conditions can play a central role in laser induced desorption.[2–8] The use of ultrafast vibrational spectroscopy to resolve the specific states of molecules is particularly attractive for detailed descriptions of molecular environments before and after a reaction. Thus far most measurements of this nature have focused on vibrational energy relaxation of molecules on surfaces, and have relied on the use of resonant IR pump pulses to create nonequilibrium populations in specific bonds.[9–13] In these experiments energy flows from the excited adsorbate to the unperturbed substrate reservoirs. An alternate approach to measuring adsorbate-substrate coupling, is to deposit energy into the substrate and monitor energy flow into and out of the adsorbate.[4,14–16] It is this method of studying adsorbate vibrational dynamics, and the particular application to the CO/Cu(111) system, which forms the subject of this review.

How do simple vibrating molecular adsorbates respond to ultrafast substrate heating? In what ways are IR probes sensitive to these phenomena? In Sec. 2 we review the basics of IR spectroscopy on metal surfaces, and then develop a description for the frequency-dependent temporal response of an adsorbate, that accounts for variations in adsorbate complex frequency and population. The formalism enables us to predict the response of the adsorbate to various excitations and to compare experimental methods.

In Sec. 3 we describe the metal substrate response to the ultrafast visible heating pulse. A two-temperature model[17] will be reviewed and discussed in context of the present experiment. The model enables us to compute the bulk electron temperature and the bulk phonon temperature following the absorption of energy from the visible pulse. The resulting

temperature reservoirs will subsequently be coupled to the adsorbate.

The adsorbate responds to rapid changes in the substrate temperature in various ways. These include variation in IR absorption strength, and temperature-dependent spectral effects such as the shifting of vibrational frequencies and line broadening. These latter processes can arise when the observed high frequency mode is anharmonically coupled to a low frequency mode. In Sec. 4 we outline an exchange theory which has been successfully applied to account for the observed temperature-dependent steady-state response of adsorbed CO. We develop a related description based on a stochastic Brownian oscillator model to account for our time-resolved studies.

Experimental details are described in Sec. 5, and the results and implications of our measurements are discussed in Sec. 6. In particular we find that at low levels of visible-pulse excitation the spectral variation of the CO stretch vibration is produced via the heating of the frustrated translational mode of the adsorbate. The molecular temperature is determined and, interestingly, is found to be greater than the bulk electron and phonon temperatures over certain time scales. At higher excitations, deviations from the model are observed. In general, at excitation levels nearly sufficient for desorption, temperature dependent coupling rates may arise. Temperature-dependent extensions of the exchange model will be discussed.

2. Vibrational Response of Surface Adsorbates to Infrared Probes

The vibrational response of an adsorbate on a metal surface provides information about the orientation, site, temperature, interactions, and number density of the species. In our experiments we probe the internal stretch vibration of CO molecularly adsorbed on Cu(111). Since CO adsorbs with its dipole moment perpendicular to the metal surface and since s-polarized fields above a conducting surface are suppressed, we will focus our discussion on reflectivity changes associated with the p-polarized component of our incident beam. We will further assume that the polarization produced in the adsorbate monolayer depends linearly on the electric field *in the layer*. In general the molecules in the layer interact with one another. Nevertheless, for most of our discussion we will consider the monolayer to be a collection of independent damped oscillators.

We shall see that our spectroscopic measurements are particularly sensitive to changes in the molecular lineshape including oscillator frequency and damping. Changes in magnitude, brought about by variations in adsorbate population or oscillator strength, may also be observed. In this section we will review the salient features of steady-state IR spectroscopy, and then we will extend the discussion to encompass time-resolved reflection measurements. In the process we will consider several approaches to time-resolved experiments, and the information contained therein. Finally, we will touch on some of the complications that can arise in time-resolved experiments on surfaces particularly as a result of temperature-dependent changes in the underlying bulk material.

2.1. *IR Reflection Absorption Spectroscopy: CW Results*

The adsorbate/metal system is often modeled as three adjoined layers. Reflection spectroscopy in this case has been treated by several authors.[18–20] Here we will summarize the development in Ref. 20. As depicted in Fig. 1, we consider the adsorbate layer with dielectric constant ε_3, to be sandwiched between two semi-finite layers: vacuum with dielectric constant ε_1, and metal with dielectric constant ε_2. We are interested in the reflectivity change of the p-polarized component of the incident IR beam. The effect of the adsorbate layer is considered weak and is treated as a perturbation.

Generally an incident field of the form,

$$E_0(t) = \mathcal{E}_0 e^{i(\mathbf{k}_1 \cdot \mathbf{r} + \omega t)}, \tag{1}$$

with wave vector $\mathbf{k}_1$ and carrier frequency ω, impinges on the sample. The basic plan is to compute the electric field above the surface, the adsorbate polarization in the monolayer, and then the field radiated by this polarization. The field *in the monolayer* is approximately the sum of the incident and reflected fields just above the metal surface. This driving field will depend on the incident angle of the IR beam, and the p-polarized complex reflection amplitude, r_p (i.e. Fresnel amplitude). For the particular case of noninteracting CO on Cu(111), the z-component of monolayer polarization perpendicular to the surface is of the form,[19]

$$P_z = \chi_\perp E_0 (r_p + 1)(k_{1z}/k_1), \tag{2}$$

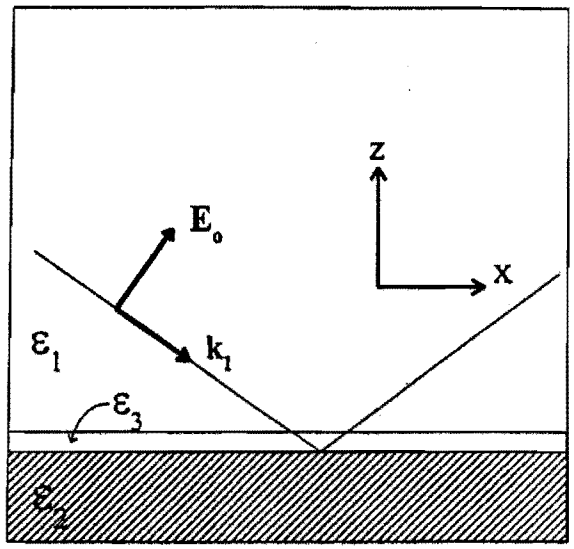

Fig. 1. Reflection of the incident IR field $E_0(t) = \mathcal{E}_0 e^{i(\mathbf{k}\cdot\mathbf{r}+\omega t)}$ from the adlayer and metal substrate is treated with a three layer model. The adsorbate with dielectric constant ε_3 is sandwiched between the vacuum with dielectric constant ε_1 and the metal with dielectric constant ε_2. The field in the monolayer is determined by $E_0(t)$ and the substrate reflectivity. The total reflected field is the sum of $r_p E_0 t$ and the specular field reradiated by the induced adlayer polarization.

where $\chi_\perp$ is the CO adlayer susceptibility, r_p is the p-polarized reflectivity of the metal in the absence of the adlayer, and k_{1i} is the ith component of $\mathbf{k}_1$. The reradiated field in the specular direction due to a thin sheet of polarization P_z (Ref. 19) is,

$$E_{\text{ads}} = \left(\frac{i4\pi k_1}{\varepsilon_2 k_{1z} + \varepsilon_1 k_{2z}}\right)\left[\frac{\varepsilon_2}{\varepsilon_3} k_{1x} P_z\right] . \tag{3}$$

The *total* reflected field is simply the sum of the reflected field in the absence of the monolayer, i.e. $E_p = r_p E_0$, plus the adsorbate field E_{ads}. In the small signal limit, the differential p-polarized reflectivity is,

$$\frac{\Delta R}{R} \cong -2\text{Im}(G\chi_\perp) , \tag{4}$$

where

$$G = \frac{8\pi k_{1z} k_{1x}^2}{k_{1z}^2 - (k_1/k_2)^4 k_{2z}^2} . \tag{5}$$

The angular-dependence of the signal is determined by G (Fig. 2). To a first approximation G can be considered completely real and $\Delta R/R$ is linearly proportional to the imaginary component of the adsorbate susceptibility. However, for high incident angles (i.e. 89° for Cu) G can be 10% imaginary [Fig. 2(b)] and therefore $\Delta R/R$ is a mixture of the real and imaginary components of the adsorbate susceptibility. In our experiments with $\theta_{\text{incident}} \leq 85°$, G is $\geq 97\%$ real.

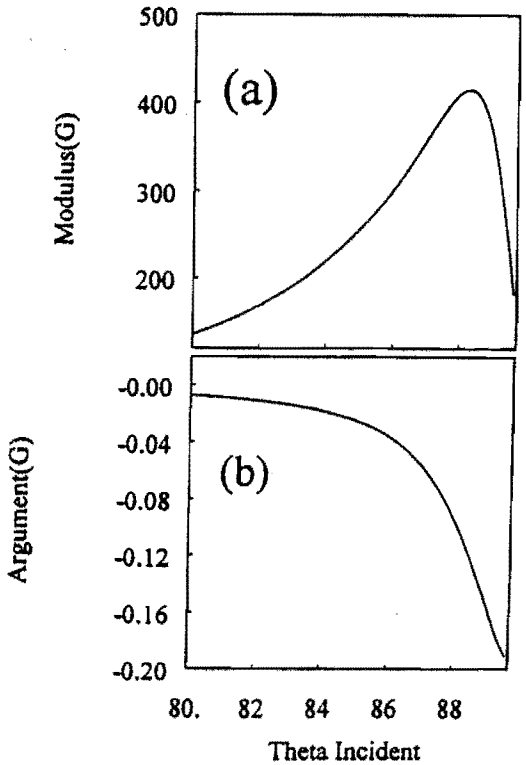

Fig. 2. The function G determines the Θ_{incident} dependence of $\Delta R/R$, the adlayer absorption signal. Using optical coefficients of Cu the modulus (a) and argument (b) of $G = |G|e^{i\theta}$ were calculated.

In pump-probe experiments, particularly at high fluence, one must be careful to include all potential changes in G induced by the pump pulse. These include rapid changes in dielectric constants due to their temperature-dependence. We will consider these effects in more detail in Sec. 2.3.2.

2.2. *Time-Resolved IR Probes and the Adsorbate Vibrational Response*

Ultrafast laser pulses that are shorter than the vibrational dephasing times of condensed phase systems are quite common. For example, spectral linewidths of vibrational transitions in the steady state are usually narrower than ca. 20 cm^{-1} corresponding to dephasing times longer than 500 fs. If vibrational states are caused to undergo changes on time scales less than 500 fs, it is evident that the interplay between the vibrational dephasing and the dynamical processes of interest must be considered as part of the interpretation of the experiment. In the particular case of CO on Cu(111) the free induction decay time, as measured by sum-frequency generation (Ref. 21) is $T_2 = 2.2$ ps. This section addresses some issues related to the probing of perturbed vibrational transitions using ultrashort pulses. There are a variety of possible approaches to obtaining transient IR spectra and the experimental manifestations of the vibrational dephasing are dependent on the method used. Two extreme approaches used in the study of IR transients are the conventional pump/probe method (see for example Refs. 9, 13), which uses short light pulses to pump and probe the sample, and the quasi-CW method (see for example Refs. 22, 23) which uses ultrafast gated IR detection. These approaches generally yield different signals from the same sample so that a comparison of the advantages and disadvantages of each of them is considered worthwhile.

The simplest approach to calculating time-dependent vibrational spectra is to solve the damped Liouville equations (Bloch equations) for a two level system with Hamiltonian:

$$\mathcal{H} = \mathcal{H}_0 + S(t) + V(t)\,, \tag{6}$$

where $\mathcal{H}_0$ is a two-level system with Bohr frequency $\omega_{10} = \omega_1 - \omega_0$ which in the present case will be a vibrational frequency. $S(t)$ is a time-dependent perturbation such as a first-order Stark effect that will usually be slowly acting compared with $V(t)$, the interaction of the two-level system with an

electromagnetic field $E(t)$: i.e.

$$V(t) = -\mu_{01} E(t), \tag{7}$$

where the field magnitude is $E(t) = \mathcal{E}(t)\cos(\omega t)$. The system is considered to be in contact with thermal reservoirs and the relaxation processes are introduced phenomenologically.

The Liouville equation for the off-diagonal elements of the density matrix in the representation of $\mathcal{H}_0$ or $\mathcal{H}_0 + S(t)$ is written with a time-dependent dephasing rate $\Gamma(t)$ as follows:

$$\dot{\rho}_{01} = \frac{i}{\hbar}[\rho, \mathcal{H}]_{01} - \Gamma(t)\rho_{01}\,. \tag{8}$$

Equation (8) can be integrated (see Appendix A and comments below) to yield:

$$e^{-i\omega_L t}\rho_{01}(t) = -\frac{i\mu_{01} n_0(t)}{\hbar} \times \int_{-\infty}^{t} dt_1 \mathcal{E}(t_1) e^{\left(i\Delta_{01} + \gamma_0)(t_1 - t) - \int_{t_1}^{t} d\tau [i\Delta S_{01}(\tau) + \gamma(\tau)]\right)} \tag{9}$$

where $\Delta S_{01}(\tau) = \frac{1}{\hbar}[S_{00}(\tau) - S_{11}(\tau)]$ represents the time-dependent Stark shift and $\Delta_{01} = \omega_{01} + \omega_L$ is the zero-order detuning in the rotating wave approximation. The parameter $\Gamma(t)$ has a time-dependent part $\gamma(\tau)$ to account for any changes in the bath to which the system is coupled, as well as a time-independent part γ_0. The t dependence in the ground state population $n_0(t)$ allows for the effects of the optical field bleaching the population *and* the coherence which are *not* included in (8). Bleaching in this context means a diminishing of the generated polarization at frequency ω_L. This can occur for example when the optical excitation generates a new population with no new coherence in the system. Any population in $v = 1$ of the CO stretch is ignored, but will be considered later. The $n_0(t)$ in Eq. (9) accounts only for the changes of population arising from light induced desorption and not excitation to other vibrational states. The changes in the propagator in Eq. (9) are initiated by optical excitation of electron hole pairs in the metal. Since the dephasing time for the electron hole pairs is extremely short (< 20 fs), there is virtually no contribution to the signal from IR fields coupling to the system *during* this excitation process.

This is an important condition under which Eq. (9) will be evaluated: It will be assumed to include only two time orderings: one with the probe field coupling before, and the other with the probe field coupling after the externally induced changes in complex frequency. In Sec. 4 a more fundamental justification of Eq. (9) is given by means of a stochastic model for the dynamics.

The purpose now is to compare two different experimental approaches to measuring $\rho_{01}(t)$ or its spectra. We defer the inclusion of substrate effects to Sec. 2.2.1 and consider *here* a sample probed in *transmission*. When infrared light pulses are employed in the experiment, the envelope $\mathcal{E}(t)$ is finite and presumably has a width shorter than the dynamics of interest. On the other hand, with the gating technique the IR field is quasi-monochromatic and $\mathcal{E}(t) = \mathcal{E}_0$ is effectively a constant over the time scale of the experiment.

First, the gating technique (9) is considered: The CW or quasi-CW infrared beam is gated by up- or down-conversion in a nonlinear crystal after the sample by mixing with a short pulse having field envelope $\mathcal{E}(t-t_g)$ centered at the gating or delay time t_g. Thus if the signal is small, the current in the square law photodetector is proportional to:

$$\langle \mathcal{E}^2(t-t_g)[\mathcal{E}_0 + \mathcal{E}_{\rm gen}(t)]^2 \rangle \,, \tag{10}$$

where $\mathcal{E}_{\rm gen}(t)$ (to be distinguished from the complex $E_{\rm ads}$ which explicitly accounts for the reflection geometry) is the in-phase part of the IR field generated at time t by the polarization derived from $\rho(t)$ given in Eq. (9). The angle brackets denote time average. Note that if the gating pulse is very short compared with the relevant dynamics, and if signal is small then the detected light intensity is given approximately by:

$$I(t_g) \propto \mathcal{E}_0^2 + 2\mathcal{E}_0\mathcal{E}_{\rm gen}(t_g) \,. \tag{11}$$

It follows that the difference between the signals under pumped and unpumped conditions is just proportional to $\mathcal{E}_{\rm gen}(t_g)$ which is obtainable directly from Eq. (9) with $t = t_g$ and $\mathcal{E}(t) = \mathcal{E}_0$. The cosine, or in-phase part of the generated field enveloped is proportional to $\mathrm{Im}\{\rho_{01}e^{-i\omega t}\}$, so for the CW method the field is, apart from constants,

$$\mathcal{E}_{\rm gen}(t) = \mathrm{Im}\left\{ \mathrm{in}_0(t) \int_{-\infty}^{t} dt_1 e^{-\int_{t_1}^{t} \Omega_{01}(\tau)d\tau} \right\} , \tag{12}$$

where we replaced the complex frequency in the exponent of Eq. (9) with $\Omega_{01}(\tau) = (i\Delta_{01} + \gamma_0) + i\Delta S_{01}(\tau) + \gamma(\tau)$.

The situation for a pump-probe signal is qualitatively different from Eq. (12). The relevant part of the generated field is still $\mathrm{Im}\{P(t)e^{-i\omega_L t}\}$ which is obtained from Eq. (9) using $P = \mathrm{Tr}\{\mu\rho\}$ but an explicit form for $\mathcal{E}(t)$ is required. With a filter in front of the detector enabling only the frequencies near ω_F to be measured, the signal current is equal to the product of the Fourier transforms of the probe and generated fields at ω_F. In otherwords, the spectrum of the generated field is given by the Fourier transform of $\mathrm{Im}\{\rho_{01}e^{-i\omega_L t}\}$. The pump/probe signal, apart from constants, is thus given by:

$$\frac{\Delta I}{I} = -2\mathrm{Re}\left\{ \frac{\mathcal{E}_{\rm gen}(\omega_F)\mathcal{E}(\omega_F)}{|\mathcal{E}(\omega_F)|^2} \right\} , \tag{13}$$

where ω_F is the filter frequency. These quantities are easily calculated numerically for arbitrary pulses and functions $S(t)$ and $\Gamma(t)$, but the basic properties and limitations for time domain experiments are more clearly exposed by considering δ-function probe pulses as discussed below.

2.3. *Discussion: Model of an Impulsive Perturbation*

The analysis described above is readily demonstrated for a specific model that has applications in surface experiments involving hot electrons. The sudden alteration in the properties of the electron bath might result in concomitant changes in the population of the levels of the C-O vibrator and of the spectral width and shape of the $v = 0$ to $v = 1$ transition that is being probed. As has been discussed previously, the signal at the C-O, $v = 0 \rightarrow v = 1$ transition will exhibit a variation that follows the rate of change of the population $n_0(t)$. If this change were to occur on the time scale of the pulse width of the light field that is heating the electrons, it could be seen as essentially an instantaneous loss of absorption in our experiment. Such *instantaneous* changes, could be brought about by photodesorption or, if the oscillator is sufficiently anharmonic, by electron induced vibrational excitations. These effects are clearly absent from the spectra of CO on Cu(111) presented in Sec. 6.

In the present experiments, the spectral shift and broadening brought about by the initially excited electron gas requires a deeper analysis as do the effects of population changes without desorption. Suppose the CO

resonance has a width γ_0 prior to heating the electrons and that the width is altered to γ_1 immediately after the electrons are heated. We also include the possibility that the detuning is immediately altered from Δ_{10} to Δ'_{10}. "Immediately" in this context means faster than could be measured. Delta function pulses are used to simplify the picture but without loss of the significant physics. The quasi-CW method yields a spectrum of the form given by Eq. (12) with n_0 constant. With the conditions of δ-function pump and gating pulses the differential reflectivity signal in the CW experiment is readily obtained from Eq. (12):

$$\mathrm{Re}\left\{\left(\frac{1}{\Omega_1}-\frac{1}{\Omega_0}\right)\left[1-e^{-\Omega_1\tau_d}\right]\right\}, \tag{14}$$

where $\Omega_0 = i\Delta_{01} + \gamma_0$ and $\Omega_1 = i\Delta'_{01} + \gamma_1$ are the complex frequencies before and after heating the electrons. The delay between pump (t) and gating (t_g) pulses is τ_d. This result is specifically for $\tau_d = t_g - t_p \geq 0$. Prior to $\tau_d = 0$, the absorbance or reflectance *change* is zero. Equation (14) determines how quickly the new signal can be observed and how suddenly the original absorbance characterized by Ω_0 can disappear as a result of the propagation of the complex frequency. Notice that the dynamics are determined by the *new* complex frequency.

The pump-probe method, Eq. (13), with selection of a frequency initially detuned by complex frequency Ω_0 from resonance, yields the signal intensity as follows:

$$\mathrm{Re}\left\{\left(\frac{1}{\Omega_1}-\frac{1}{\Omega_0}\right)e^{\Omega_0\tau_d}+\left(\frac{1}{\Omega_1}-\frac{1}{\Omega_0}\right)\right\}, \tag{15}$$

where the first term is for negative delay times (τ_d = probe-pump) and the second term is exclusively for the situation that the probe arrives after the pump. The first term of Eq. (15), and hence time-dependence of these signals, always grows in with time constant determined by the *unperturbed* resonance frequency Ω_0 and the peak signal occurs at zero delay of pump and probe pulses.

The significant differences between Eqs. (12) and (13) or (14) and (15) are most readily seen by diagrams representing these processes as shown in Fig. 3. In each case, the evaluation of the integral in Eq. (9) for delta function probe and gating pulses requires consideration of three regions. Region 2 where the probe field couples before the pump and is gated

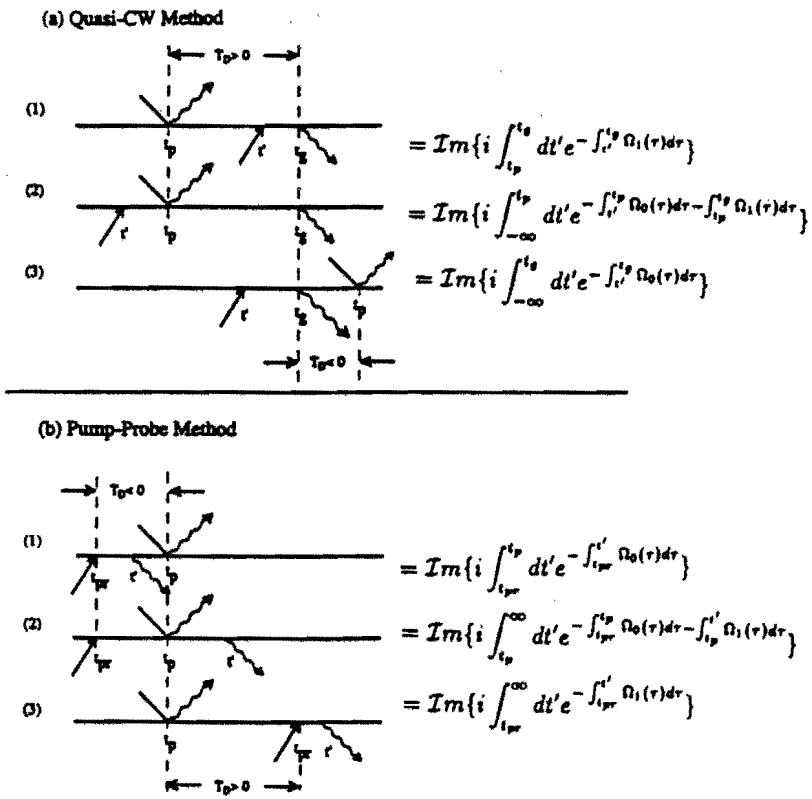

Fig. 3. Time ordering of the integrals for the impulsive perturbation model. t' is the integration variable and t_p is the arrival time of the pump pulse. (a) Quasi-CW method: The delay time, T_d, is measured between the pump-pulse, and t_g the time at which the gate pulse up-converts the IR probe. (b) Pump-Probe method: The delay time is measured between the pump-pulse and t_{pr}, the time at which the IR probe pulse impinges upon the sample.

(Fig. 3a.2) or detected (Fig. 3b.2) after the pump. Regions 1 and 3 where the probe field is coupled and gated or detected either before or after the pump. In the quasi-CW case the integral only extends up to the gating time. In the pump-probe experiment the detector senses the free induction decay (FID) radiated starting from the arrival time of the probe (t_{pr}) up to infinity. Diagrams 3b.1 and 3b.2 correspond to the FID of the unpumped

sample being perturbed by the pump at t_p. In that case, the system propagates with complex frequency Ω_0 from t_{pr} to t_p and with complex frequency Ω_1 from t_p to t' and the detector response results in an integration over t'. In the quasi-CW method the signal begins to change after the pump arrives.

Consider some qualitative features of the two approaches. The pump probe signal evolution is always shaped initially by the unpumped vibrational properties in Ω_0. On the contrary, the time-dependence of the quasi-CW signal is determined by Ω_1– the *new* spectrum. Fig. 4(a) shows the signals expected for the case where the absorption width is suddenly increased. The only effect this increase has on the pump-probe signal is on its amplitude at zero delay. On the other hand, the CW method yields a signal growth kinetics that depends on the amount of line broadening that occurred. In another example, the probe is chosen on resonance with the unperturbed system and the perturbation causes an instantaneous line shift Fig. 4(b). Again the pump-probe signal (bleach) grows up to zero delay in accordance with $e^{\gamma_0 \tau_d}$ and is constant thereafter at a level determined by the magnitude of the frequency shift. A quite different response is expected from the quasi-CW method which will exhibit damped oscillations with period corresponding to the frequency mismatch. If this shift is sufficiently large enough so that the time resolution is insufficient to isolate the beats or if the sample is sufficiently inhomogeneous, then an instantaneous change in absorbance will be sensed. An example of this effect was observed in the experiment on the photodissociation of carbon monoxide from an iron carbonyl.[24] On dissociation, the resonance frequency shifts in about 50 fs from 1951 cm^{-1} to 2135 cm^{-1} without much change in width. This shift of 184 cm^{-1} corresponds to a beat period of 180 fs which could not have been resolved in that experiment so an "instantaneous" bleach signal is observed. An changes of integrated absorption cross-section that occur as a result of the perturbation must also be included in the evaluation of the responses. These appear in much the same way as the population changes in Eq. (9). This is an example where the population kinetics give a reasonable interpretation of spectral changes.

The comparison shows the advantage of the quasi-CW method when the experimental objective is to study the change in position or width of an existing absorption without population changes; the kinetics of the change can be observed without direct interference from the free induction

decay of existing absorption. For example if an absorption band is instantaneously bleached, perhaps by a photochemical reaction that removes the species, the observed response is immediate. On the other hand, the pump-probe method has a clear advantage when the signal is a new absorption introduced by the pumping process. The pump-probe technique is capable of tracking processes much faster than the equilibrium dephasing times when there is no requirement to single out a particular frequency, i.e. when no filter or monochromator is placed in from of the detector. Consider a transition having a typical vibrational width of 10 cm^{-1} that is

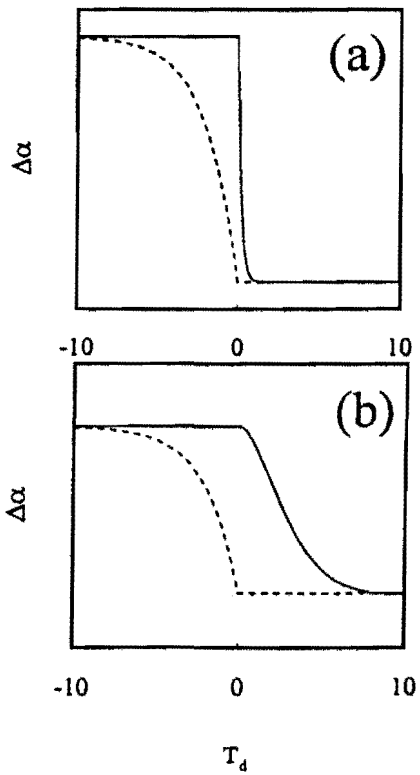

Fig. 4. Simulation of the difference between signals expected for pump-probe (dashed line) and quasi-CW gated method (solid line). (a) Signals for instantaneous line broadening, in this example $\gamma_1 = 5 * \gamma_0$ and $\omega_L = \omega_0$. (b) Signals for an instantaneous shift by 2 cm^{-1} with $\omega_L = \omega_0$ and $\gamma_1 = \gamma_0$.

shifted by 100 cm^{-1}, but whose stationary width is unchanged as a result of a pumping process. If the shift is essentially immediate the signal at the new frequency grows in with time constant $T_2 = 2.2$ ps if a filter is placed in front of the detector. However, without the filter and detecting all the frequency components, the signal will track the profile of the probe pulse. At times much less than the dephasing time the field corresponding to the new transition is distributed over a broader frequency region, but the probe pulse itself is by definition spectrally broad enough to detect the whole absorption on the time scale of the pulse width.

Optical excitation of the surface can lead to a redistribution of population amongst the modes of the adsorbate surface complex. We consider here, the case where the $v = 1$ state of the CO stretch is populated at the expense of $v = 0$. In this case, the generated field consists of additional contributions corresponding to transitions from $v = 1$ to $v = 0$ and $v = 2$. Assuming $n_1(t)$ is the population in $v = 1$ at time t, the generated field is:

$$\mathrm{Im}\left\{ i \int_{-\infty}^{t} dt' \left[n_1(t') e^{-\int_{t_1}^{t} \Omega_{12}(\tau) d\tau} + \left\{ n_0(t) - \gamma_1 \int_{t'}^{t} n_1(\tau) d\tau \right\} e^{-\int_{t_1}^{t} \Omega_{01}(\tau) d\tau} \right] \right\}, \tag{16}$$

with the same notation as in Eq. (12) and where γ_1 is population relaxation rate from $v = 1$ to $v = 0$. This predicts a part that follows the pump pulse and a slower response with magnitudes dependent on the difference between the complex frequencies Ω_{01} and Ω_{12}.

Before concluding our discussion of the optical response we will consider two additional extensions to our model: effects due to a time-dependent substrate reflectivity, and a manifestation of the exciton nature of the adsorbate stretch vibrational excitation.

2.3.1. *Static and Time Variant Substrate Reflectivity*

The time-resolved results of the previous section can be incorporated into the description of reflection absorption spectroscopy from Sec. 2.1. For the gated CW probe method, we first consider the case of static substrate optical properties. Introducing a time-dependent adsorbate susceptibility $\chi(t)$ the total field can be written,

$$E_{\mathrm{tot}} = r_p E_0 [1 + iG\chi(t)]. \tag{17}$$

Here, the parameter G accounts for the adsorbate geometry and is defined by Eq. (5). The time-dependent susceptibility $\chi(t)$ is obtained by dividing the adsorbate polarization $P(t)$, by the driving field and can be expressed in a form similar to Eq. (12),

$$\chi(t) = i \frac{\mu_{01}^2 n_0(t)}{\hbar} \int_{-\infty}^{t} dt_1 e^{-\int_{t_1}^{t} \Omega_{01}(\tau) d\tau}. \tag{18}$$

In the pump/unpump scheme, the differential reflectivity will be,

$$\left(\frac{\Delta R}{R}\right)_{\mathrm{pump}} - \left(\frac{\Delta R}{R}\right)_{\mathrm{unpump}} = 2\mathrm{Im}\{G(\chi(t) - \chi_0)\}. \tag{19}$$

Note that when G has a significant imaginary component the signal will be proportional to a mixture of the imaginary *and real* components of $\chi(t)$.

When heated by a visible pulse the dielectric constant of the underlying metal will change. For example, a change of temperature from 72° K to 275° K produces a 3% change in reflectivity at $\Theta_{\mathrm{incident}} = 72°$. Ultimately a complete description of the total reflected field $E_{\mathrm{tot}}(t) = E_p(t) + E_{\mathrm{ads}}(t)$ must account for the time variance of *both* the substrate optical properties and the adsorbate layer polarization. We will estimate the effect of changes in substrate reflectivity below. Following the development of Sec. 2.2 we assume a small time-dependent component to the reflectivity amplitude,

$$r_p(t) = r_p[1 + \zeta(t)]. \tag{20}$$

Using the wave vectors $\mathbf{k}_1$ and $\mathbf{k}_2$ for the field in vacuum and in metal respectively, the time-dependence of the substrate optical response can be described in terms of a fractional change $\frac{\delta k_2(t)}{k_2}$ in complex k_2, i.e.

$$\zeta(t) = \left[\frac{k_2}{r_p}\frac{\partial r_p}{\partial k_2}\right]\frac{\delta k_2(t)}{k_2} = \left[\frac{2k_2^2 k_1^2 k_{1z}(2k_{2z}^2 - k_2^2)}{k_{2z}(k_2^4 k_{1z}^2 - k_1^4 k_{2z}^2)}\right]\frac{\delta k_2(t)}{k_2}. \tag{21}$$

The adlayer polarization $P_z = N\mathrm{Tr}\{\mu\rho\}$, can be calculated as in Sec. 2.3, with the time evolution of ρ obtained from the integrated Liouville Eq. (9), with the driving field,

$$E_z(t) = E_0(t)\{1 + r_p[1 + \zeta(t)]\}\frac{k_{1z}}{k_1}. \tag{22}$$

Two different aspects of the reflection geometry which are combined in the function G have different time-dependences. One factor which relates

the incident field, E_0, to the driving field, E_z, must be convoluted with the adsorbate response. The other factor which relates the adsorbate polarization to the specularly reradiated field is considered to have an instantaneous effect on the reradiated field. These two factors must therefore be treated separately in considering a time-dependent substrate optical response. We introduce the function $H(t)$ to relate the adsorbate polarization to the specularly reradiated field. $E_{\rm tot}$ can be written,

$$E_{\rm tot}(t) = r_p[1 + \zeta(t)][E_0 + iH(t)P_z(t)]\,, \tag{23}$$

where

$$H(t) = [1 + \eta(t)]\left\{\frac{4\pi k_1 k_{1x} k_2^2}{k_2^2 k_{1z} - k_1^2 k_{2z}}\right\}\,, \tag{24}$$

and

$$\eta(t) = \left[\frac{k_1^2(k_2^2 - 2k_{2z}^2)}{k_{2z}(k_2^2 k_{1z} - k_1^2 k_{2z})}\right]\frac{\delta k_2(t)}{k_2}\,. \tag{25}$$

In Eq. (24) we have accounted for the change in dielectric constants of the metal through $\eta(t)$, which is the same order of magnitude as $\zeta(t)$. From Eq. (23) one can see that the leading contribution to $E_{\rm tot}$ due to changes in substrate reflectivity is $\zeta(t)r_pE_0$. This term *does not* involve the adsorbate polarization. The terms which modulate the adsorbate polarization are at least an order of magnitude smaller. Keeping only the $\zeta(t)r_pE_0$ term, the total reflected field can be written,

$$E_{\rm tot} = r_pE_0[1 + \zeta(t) + iG\chi(t)]\,. \tag{26}$$

For a pump/unpump scheme the difference signal will be,

$$\left(\frac{\Delta R}{R}\right)_{\rm pump} - \left(\frac{\Delta R}{R}\right)_{\rm unpump} = 2{\rm Re}\{\zeta(t) + iG(\chi(t) - \chi_0)\}\,. \tag{27}$$

The magnitude of the effect due to temperature-dependent substrate optical properties can be estimated by tuning the probe laser far from the CO stretch resonance, measuring $\zeta(t)$ directly. In our low fluence experiments ($F_{\rm abs} = 0.09$ mJ/cm^2) we have not observed any changes in reflectivity far off resonance. However in the case of CO on Pt(111) the changes in substrate reflectivity were the same size as the differential signals induced in the adsorbate absorption.[15]

2.3.2. *Excitonic Nature of the Oscillators*

The exciton nature of the adsorbed CO oscillators has several possible effects not included in a two-level single oscillator description. Most notably, population of the first excited state does not have a simple bleach signature. Instead, the fundamental adsorption can shift linearly with the population of the first excited state and overtone or two-phonon bound state absorptions may occur.[25] Some of these effects have been observed experimentally. In the case of CO on Pt(111) time-resolved spectra of the CO stretch revealed a shifting absorption following resonant IR excitation.[10] The results were interpreted with a model for strongly coupled anharmonic oscillators. For H on Si(111) a localized two-phonon bound state absorption was observed.[26] The nature of adsorbate excitations can therefore be both collective and phonon-like or localized on single molecules. In the present measurements however, the expected excitation of the CO stretch remains below 1% (see Sec. 4.3) and we are not sensitive to these phenomena.

3. Response of the Bulk to Ultrashort Pulse Heating

The dynamics of adsorbates becomes particularly interesting when ultrashort laser pulses are used to excite the underlying substrate. This is because, on very short time scales, it is possible to excite the pure electronic degrees of the solid before energy can be substantially exchanged with the phonon degrees of freedom of the solid. Eventually, we expect the electron and phonon temperature reservoirs to equilibrate, however just after excitation a unique environment can be created for the molecule in which the substrate electron and phonon temperatures are vastly different. These conditions cannot be achieved through conventional thermal heating processes.

In the present paper we are concerned with the variation of adsorbate vibrational spectra just after substrate excitation. This response will depend on the coupling between the adsorbate vibrations and the near surface bulk phonon and electronic excitations. The population of the adsorbate-like modes induced by these bulk excitations will depend on the temperature of the respective substrate reservoirs. We briefly review the conventional wisdom[17,27–34] regarding these temperature variations.

The initial interaction of the substrate with the visible electromagnetic field produces a hot electron-hole plasma. This highly nonequilibrium distribution of electrons and holes will thermalize in less than a picosecond.

For some metals such as Au, this thermalization time can be as long as 600 fs (Ref. 34), however for Cu this time is estimated to be about 70 fs (Ref. 5). Our pulses of ≈ 300 fs duration enable us to treat this electronic thermalization as essentially instantaneous. Once the electrons have thermalized, the cooling problem can be considered in the context of a classical heat flow model first suggested by Anisimov.[17] In this model the cooling of electrons occurs via energy transfer to the phonons through electron–phonon collisions and via heat conduction away from the surface. These equilibration processes are fast, but before the two reservoirs thermalize, the electrons can reach peak temperatures much greater than those of the phonons. The coupled differential equations that describe these processes are as follows:

$$C_e(T_e)\frac{\partial T_e}{\partial t} = \nabla(\kappa_e \nabla T_e) - g(T_e - T_l) + S(z,t)\,, \tag{28}$$

$$C_l\frac{\partial T_l}{\partial t} = -g(T_l - T_e)\,. \tag{29}$$

Here, a source term $S(z,t)$ accounts for the initial deposition of heat by the light pulse, and is assumed to interact with the electrons only. The electrons have a heat capacity $C_e = \gamma T_e$, and are subject to thermal diffusion characterized by κ_e, and energy loss to the phonons at a rate g. The phonons, with heat capacity C_l, relax towards the electronic reservoir temperature also with rate g. Diffusion of energy through phonon mechanisms is negligible on these time scales and is ignored here.

The problem can be treated in three dimensions. In our experiments however, the beam waists of ~ 100 μm were $\geq 10^3$ times the optical skin depth and electron diffusion length. In this case the temperatures can be considered homogeneous in the plane of the crystal surface and the diffusion problem is effectively one-dimensional. Using the appropriate boundary conditions we have solved these equations numerically for our system parameters (see Fig. 5). For a fluence absorbed of $F_{abs} = 0.09$ mJ/cm^2 the electrons have a temperature rise $\delta T_e = 305$ K, which decays in ~ 1 ps primarily through heat diffusion. The phonon temperature by contrast rises more gradually by $\delta T_l = 7$ K. Since the diffusion of heat away from the surface, temperature is dominated by the electrons, T_e drops slightly below T_l and both temperatures return to 95 K in ≤ 1 ns.

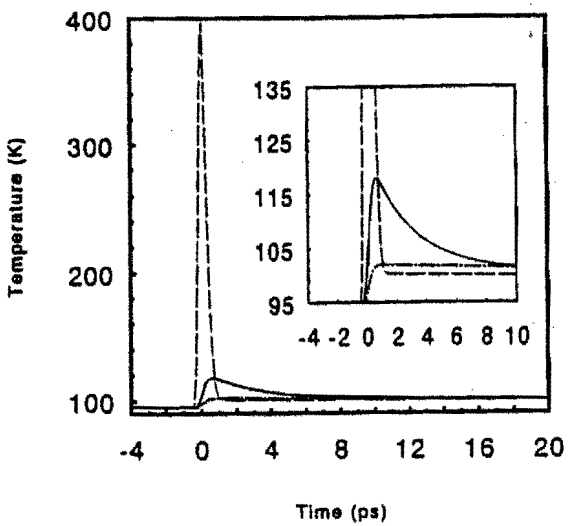

Fig. 5. Time evolution of the electron (dashed line), phonon (dot-dashed line), and adsorbate (solid line) temperatures at the surface of the Cu substrate for an average fluence absorbed of $F_{abs} = 0.087$ mJ/cm^2. Inset: Same plot on an expanded vertical scale. Note, the adsorbate temperature was obtained using the best estimates for electron and phonon coupling rates γ_e and γ_l (see text for details).

The adsorbate excitation and temperature profiles are calculated by convoluting a response function with T_e and T_l profiles. Errors in the substrate temperatures will lead to errors in our estimated adsorbate-substrate coupling rates. The accuracy of the parameters used in this problem therefore need to be considered. The best measurements for the Cu electron–phonon coupling parameter g have been derived from transient reflectivity measurements of thin Cu films where the effect of diffusion is minimized.[28,32,33] For polycrystalline Cu this value is $g = 1 \times 10^{17}$ W/m^{3}K. Grain boundaries are believed to enhance the electron–phonon scattering process, so that single crystals might be expected to have smaller values of g. For Au, a comparison of polycrystalline films to single crystal thin films has been made and the single crystal g was 10–20% smaller than the polycrystalline sample.[33] The diffusion constant κ_e, has been treated in different ways, both as temperature-dependent and temperature-independent. Here we have assumed the temperature-dependence arises from a Sommerfield

model[5,29] of the form,

$$\kappa_e = \kappa_{e_0}(T_e/T_l)\,. \tag{30}$$

The Sommerfield model does not however account for the static temperature-dependence that has been observed in Cu.[35] C_e and C_l on the other hand are fairly well determined experimentally from 100° to 900° K (Ref. 35). Our analysis is most susceptible to changes in g. A deviation in κ changes the effective penetration depth of the visible heat source but does not greatly change the over all shape of the curves. A change of the electron–phonon coupling constant g, however, proportionally changes the decay rate of the electron temperature and thus produces an error in the determination of the coupling rates of the adsorbate to these reservoirs.

4. Coupling of Harmonic Oscillators to Electrons, Phonons, and Other Vibrations

The vibrational states of the adsorbate/surface complex are amenable to study by infrared spectroscopy. Therefore some understanding of the force field for the CO-metal unit is needed in order to establish a description of the observed transitions in the infrared. Of primary importance to the dynamics of energy flow within this unit is some notion of the anharmonic coupling between the various adsorbate-like modes and the coupling between metal-like phonons or electrons and these adsorbate modes. Table 1 lists the frequencies for the four principal modes that involve motion of the carbonyl group. There are also calculations of these frequencies[36] that lend support to the experimental mode assignments. Some knowledge of the spectroscopic parameters can be gleaned from studies of metal carbonyls,[37] however there is very little experimental information on the anharmonic coupling between the various CO-adsorbate modes.

While in general a harmonic oscillator in contact with a large number of other modes will interact with each of the modes separately, some assumptions about these couplings permit simplifications and make the system amenable for study. For example, if the other modes interact strongly with each other, but weakly and similar strength to the oscillator, then the system can be described using a single average coupling rate of the oscillator to the collective bath of modes. Such a description can be extended to include explicit anharmonic couplings, both adiabatic and nonadiabatic, with specific bath modes that couple preferentially to the oscillator. In

particular for our experiment in which we probe the CO stretch vibration, the low frequency adsorbate-like modes are included explicitly, and the metal substrate is described by electronic and vibrational baths. In this section we will outline the expected response of the C-O stretch resulting from these possible interactions with the substrate.

4.1. *General Theory of a Harmonic Oscillator Coupled to a Temperature Reservoir*

We start by reminding the reader of the manner by which a harmonic oscillator couples to a stochastic temperature reservoir. In particular we would like to derive a differential equation relating the temperature of an oscillator to the temperatures of the reservoirs. In our case there are two reservoirs (i.e. bulk electron and phonon) whose temperatures vary in different ways before equilibrating (Sec. 3). When an oscillator with average energy U_{osc}, characterized by a temperature T_{osc} (in the Bose–Einstein sense), is placed in contact with a thermal reservoir at temperature T_R, energy is exchanged until the oscillator acquires the reservoir temperature T_R. For a harmonic oscillator the time evolution of this process can be calculated explicitly and, with some reasonable assumptions has a very simple form. The calculation depends only on the oscillator frequency, the average occupation of elementary excitations in the reservoir at the oscillator frequency, and the rate γ associated with the population relaxation between the lowest two oscillator energy levels in the presence of the reservoir. For this model, γ is temperature-independent and the elementary *excitations* in the temperature reservoirs are bosons. By considering the energy flow or population transfer in and out of the ith level of a harmonic oscillator (Fig. 6) we can write the rate of change in occupation probability of the ith level, p_i as follows:

$$\dot{p}_i = p_{i-1}W_{i-1,i} - p_i(W_{i,i+1} + W_{i,i-1}) + p_{i+1}W_{i+1,i}\,. \tag{31}$$

Here $W_{i,j}$ is the rate of population transfer from the i level to the j level. We can simply calculate the rate change of the average occupation number $\bar{n} = \sum ip_i$, using $\dot{\bar{n}} = \sum i\dot{p}_i$. For a harmonic oscillator with a linear coupling to a bath at temperature T_r,

$$W_{i,i+1} = n_r\gamma(i+1)\,, \tag{32}$$

$$W_{i+1,i} = (n_r + 1)\gamma(i+1)\,, \tag{33}$$

where $n_r = \bar{n}(T_r)$, is the average occupation number for an oscillator *in equilibrium* with the harmonic bath. Substituting Eq. (32) and Eq. (33) for $\dot{p}_i$ in Eq. (31) we find that $\dot{\bar{n}}$ is,

$$\dot{\bar{n}} = \gamma\Big\{ n_r \sum_i i^2 p_{i-1} - (2n_r+1)\sum_i i^2 p_i + (n_r+1)\sum_i i^2 p_{i+1} - n_r \sum_i i p_i + (n_r+1)\sum_i i p_{i+1} \Big\}\,. \tag{34}$$

The sums can all be rewritten in terms of $\bar{n}$, p_0, and $\sum_i i^2 p_i$, which when collected, yield the simple expression,

$$\dot{\bar{n}} = \gamma(n_r - \bar{n})\,. \tag{35}$$

In the high temperature limit, Eq. (35) reduces to the form below since $\bar{n} = \frac{1}{e^{\hbar\omega/k_B T}-1}$,

$$\dot{T}_{\rm osc} = \gamma(T_r - T_{\rm osc})\,. \tag{36}$$

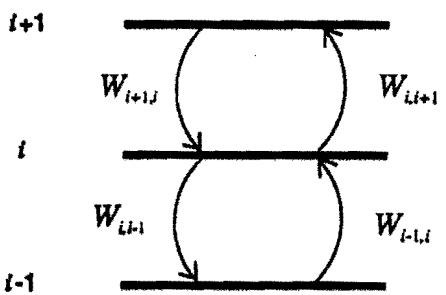

Fig. 6. Energy flow between the ith level and the nearest levels, $i-1$ and $i+1$. The individual rates $W_{n,m}$ associated with the arrows are described in the text.

In our case the oscillator can couple to phonons or electron-hole fluctuations in the bulk. The occupation of both classes of elementary excitations are described by Bose distributions at the appropriate electron or phonon reservoir temperatures T_e and T_l respectively. If we assumed the couplings

are independent of each other, then the energy flow in and out of the oscillator equals the sum of the interactions with the two baths and Eq. (35) can be extended to read,

$$\dot{\bar{n}} = \gamma_e(\bar{n}(T_e) - \bar{n}) + \gamma_l(\bar{n}(T_l) - \bar{n})\,. \tag{37}$$

In reaching Eq. (37) we have assumed that there are no off diagonal density matrix elements induced by interactions with the bath, and that the coupling to the bath is linear in the oscillator coordinate.

Table 1.

Modes	O ↕ C □	O C ↕ □	O → C → □	O → C ← □
ω	2074 cm^{-1}	330	< 60	281
γ_e	1–2 ps	(9.2)	6.3	(0.8)
γ_l	(> 1000 ps)	(9.7)	6.0	(6.0)

The normal modes of an adsorbed CO molecule. IRAS and EELS studies yield the frequencies of the C-O stretch,[56,57] The Cu-CO stretch[57,58] and the frustrated rotation (FR).[57,58] Though not measured for the Cu(111) surface, inelastic helium scattering studies determined the frustrated translation (FT) frequency for CO on Cu(100)(ω_{FT} = 34 cm^{-1}) [Ref. 15], Ni(111)(ω_{FT} = 60 cm^{-1}) [Ref. 50] and Pt(111)(ω_{FT} = 60 cm^{-1}) [Ref. 50]. An upper limit of 60 cm^{-1} therefore seems reasonable for this mode. Relaxation rates of the C-O stretch mode were determined using ultrafast IR experiments for CO on Pt(111) [Ref. 9] and CO on Cu(100) [Ref. 13]. These results can be transfered with reasonable accuracy to CO on Cu(111) [Ref. 14]. Calculations (Bracketed values) from Ref. 53 for T = 150 K were used where experimental values were not available.

4.2. *Coupling Through Low Frequency Modes*

The temperature-dependence of vibrational bands in polyatomic molecules is generally understood to arise from anharmonic coupling.[38] The molecular nuclear motions are coupled to each other and also to the bath modes. This situation permits any particular vibrational frequency to be modulated by the bath fluctuations and hence yield line-shifting and line-broadening phenomena. What is required to shift a high frequency transition is a low

frequency mode, whose occupation number is significant. The magnitude of the temperature shift or broadening will then depend on the size of the anharmonic coupling between the high and low frequency modes. The theory that describes this situation is termed exchange theory.[38,39] In the present context, we prefer to regard the dynamics in terms of Brownian oscillator models.[39,40]

The simplest type of vibrational dynamics consists of an oscillator, representing say a diatomic molecule, coupled to a bath. In this case, the temperature-dependent spectral shifts are caused by the changes in molecular potential that arise because of coupling to the motions of molecules in the bath.[38] When some modes of the bath are efficiently anharmonically coupled to the oscillator, the spectral properties of the oscillator may be described by its coupling to these modes only. The fluctuating forces due to the remaining solvent modes will then cause these coupled modes to have a stochastic behavior and hence the diatomic oscillator spectra become dependent on the correlation functions of these other modes. This Brownian oscillator model[41] would seem to have obvious utility in surface dynamics involving high frequency modes of the adsorbate, such as the CO stretch of a top site structure on a metal surface.[40] In such a case, the other modes of the top site structure (these are described in Table 1) are expected to be coupled to the stretch mode and also to the electron–phonon bath of bulk and surface states of the metal. Thus an attractive model for the temperature-dependence of the vibrational spectrum is that these bulk reservoirs cause stochastic modulation of the lower frequency modes of the adsorbate unit and that the relevant spectroscopic properties of higher frequency modes are obtained in terms of correlation functions of the lower frequency mode displacements.

In considering the relaxation of the CO stretch, in accordance with the discussion above, we treat the adsorbate modes as stochastically modulated displacements, Q_i. These few modes are considered to be Brownian oscillators satisfying Langevin equations of the type:

$$\ddot{Q}_i + \left(\frac{\alpha_i}{\sqrt{\mu_i}}\right)\dot{Q}_i + \Omega_i^2 Q_i = \frac{F(t)}{\sqrt{\mu_i}} \tag{38}$$

having frequencies Ω_i, reduced masses μ_i and damping rates α_i. Here $F(t)$ is a stochastically fluctuating force and Q_i is used as a mass weighted coordinate $Q_i^2 = \mu x_i^2$. Because of the existence of anharmonic coupling

between the CO stretch and the Q_i modes, the CO frequency and thus the density matrix elements ρ_{01} will be modulated. This is readily seen by considering the potential wells for the low frequency Q_i coordinate motion, Fig. 7: The anharmonic coupling usually causes the frequency Ω_i to be lower when the CO stretch is excited than if it is not. The actual CO stretch detuning frequency is $\Delta_{01}(Q_i) = \omega_{01}(Q_i) + \omega_L$ which for a single Brownian mode, Q, is given by:

$$\Delta_{01}(Q) = \Delta_{01} + (\zeta/\hbar)Q^2\,, \tag{39}$$

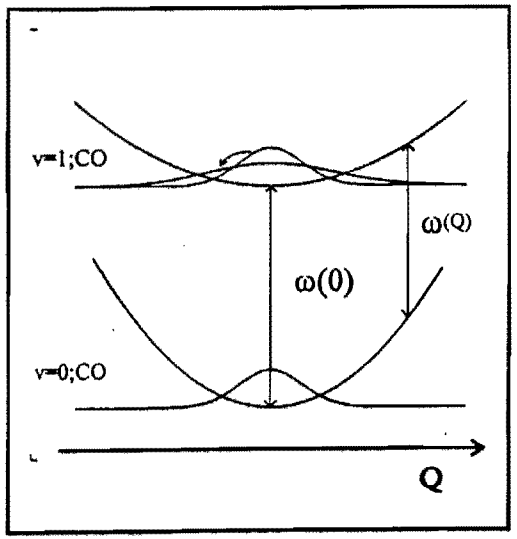

Fig. 7. Anharmonic coupling between the CO stretch and a low frequency oscillator Q_i will modulate the frequencies of both modes. The frequency Ω_i of the coordinate Q_i oscillator is determined by the width of the potential wells. The frequency $\omega(Q_i)$ of the CO stretch mode is determined by the separation of the two potential surfaces. As $\langle Q^2\rangle$ increases, the average stretch frequency decrease. Using a stochastic Brownian oscillator model the temperature-dependence of the frequency shift can be obtained explicitly (see text).

where $\zeta = \frac{1}{2}(\Omega_0^2 - \Omega_1^2)$ is a measure of the anharmonic coupling; Ω_v is the Brownian oscillator frequency in state v of the CO stretch. The pure case density matrix, σ, for the CO stretch now contains a stochastic frequency:

$$\dot{\sigma}_{01} = -\left\{ i\Delta_{01} + \gamma_0 + i\frac{\zeta}{\hbar}Q^2(t) \right\} \sigma_{01} \,. \tag{40}$$

Such a stochastic equation has the following solution (Ref. 39) for the ensemble average $\rho_{01} = \langle \sigma_{01} \rangle$,

$$\rho_{01}(t) = \rho_{01}(0) \times e^{\left\{ -i\left[\Delta_{01}t + \frac{\zeta}{\hbar}\int_0^t dt_1 \langle Q^2(t_1)\rangle\right] - \gamma_0 t - \frac{\zeta^2}{\hbar^2}\int_0^t dt_1 \int_0^{t_1} dt_2 \langle\langle Q^2(t_1)Q^2(t_1-t_2)\rangle\rangle \right\}} \tag{41}$$

or alternatively,

$$\dot{\rho}_{01} = -\{ i[\Delta_{01} + \delta(t)] + \gamma_0 + \gamma(t) \} \rho_{01} \,, \tag{42}$$

where γ_0 is the population relaxation time of the CO-stretch resulting from other mechanisms, $\delta(t) = \frac{\zeta}{\hbar}\langle Q^2(t)\rangle$ and $\gamma(t) = \frac{\zeta^2}{\hbar^2}\int_0^t dt_1 \langle\langle Q^2(t)Q^2(t-t_1)\rangle\rangle$. This result provides the propagator for the density matrix, such that in the presence of an IR driving field $\rho_{01}(t)$, is given by Eq. (9).

From Eq. (42) it is seen that the mean value $\langle Q^2(t)\rangle$ determines the shift of the stretching mode and the cumulant average $\langle\langle Q^2(t_1)Q^2(t_1-t_2)\rangle\rangle$ determines the temperature-dependent dephasing width of the transition. These averages of Q are readily obtained (Refs. 39, 40, 42) from the solutions to the Langevin equation with the assumption that the fluctuating force has no memory and there is no coupling between the parts due to electrons and nuclei, i.e.

$$\langle F(t_1)F(t_2)\rangle = 2\sqrt{\mu}\alpha k_b T \bullet \delta(t_1 - t_2) \,. \tag{43}$$

The shift and width parameters that are obtained depend on the value of $\Omega\sqrt{\mu}/\alpha$, but for the present purpose we assume the oscillator is strongly overdamped since it is then straightforward to obtain the needed high temperature results in terms of the relaxation time of the Brownian oscillator, $\beta = \Omega^2\sqrt{\mu}/\alpha$. In general the temperature of the bath, T in Eq. (42) will have a time dependence. However, here we consider the case in which variations of the bath temperature are slow compared with β, i.e. $\frac{dT(t)}{dt} \ll \beta T(t)$. The interaction of a harmonic oscillator with a harmonic bath whose temperature is rapidly varying was previously presented in Sec. 4.1. In the fast modulation limit ($\beta t \gg 1$) and small $\frac{1}{T}\frac{dT(t)}{dt}$, the line shift and line broadening can be written in terms of the bath temperature, since $\langle Q^2\rangle = \frac{k_b T}{\hbar\omega}$;

$$\delta(T) = \delta\Omega(k_B T/\hbar\Omega) \,, \tag{44}$$

$$\gamma(T) = (\delta(T))^2/\beta \,, \tag{45}$$

where $\delta\Omega \approx \zeta/\Omega$ is the change in the Brownian oscillator frequency on excitation of the CO stretch. When $\frac{1}{T}\frac{dT(t)}{dt}$, becomes comparable to β a more exact form of the line shift propagator in Eq. (9) is (Ref. 39):

$$\delta(t) = \delta\Omega(k_b T/\hbar\Omega)2\beta \int_{-\infty}^{t} dt_1 T(t_1) e^{-2\beta(t-t_1)} \,, \tag{46}$$

where $\bar{n}(t)$ is the Bose–Einstein occupation of the oscillator. These results describe a very simple situation depicted in Fig. 7. Excitation of the CO stretching mode from $v = 0$ to $v = 1$ generates a distribution of nuclear positions and velocities in the new Brownian oscillator well. The dynamics giving rise to the width and frequency changes corresponds to the evolution of this distribution into one governed by the properties of the new surface (dashed line in Fig. 8). This time-dependence is an experimental observable which, along with the effects of an underdamped oscillator coupled to the bath, is a subject of our current research.[43] In the overdamped limit this time evolution corresponds to a Kubo-like correlation function[44]; that is, a Gaussian decay at short times which tends to an exponential in the fast modulation limit or long time averaging. Clearly the oscillators in Table 1 that have been *observed* as well defined transitions are by definition not overdamped. It is therefore necessary to go further with the theory.

4.3. *Direct Electronic Excitation and Dephasing Processes*

In considering the effects of a visible heating pulse, we need also to discuss vibrational excitation and dephasing of the absorbed CO via direct interaction with the excited substrate modes. A variety of optical driven processes are possible. If localized optical excitations of CO (such as 5σ to $2\pi^*$ transition) were possible, the adsorbate would gain vibrational energy by quenching of the electronic excitations.[45–47] The energy of the incident photons however, precludes this mechanism in the present experiments. Direct coupling of either nascent or thermal electron hole pairs with the adsorbed CO can occur as the excited carriers scatter in and out of the partially occupied $2\pi^*$ orbital.[48,49] These interactions can in general induce either excited state populations or dephase the oscillators. The energy transfer rate between the C-O stretch and substrate electron hole pairs is

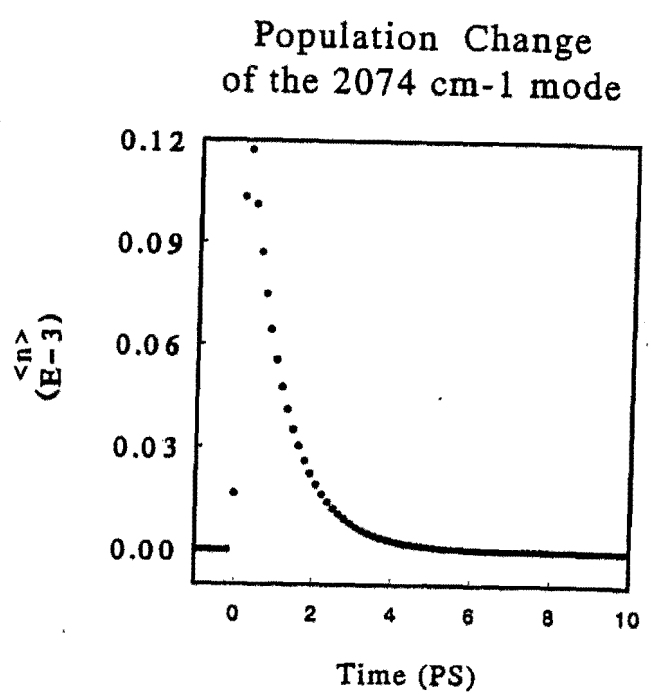

Fig. 8. Fractional population of the $v = 1$ state of the CO stretch as a function of time. Shown here is the induced population resulting from heating the Cu(111) substrate with a pulse of 300 fs duration and adsorbed fluence of $F_{abs} = 0.09$ mJ/cm^2. The calculation is described in the text.

known to be ~ 1.2 ps (Ref. 9, 13, 21). Thus, by using the rate Eq. (35) for a harmonic oscillator from Sec. 2.2 and the calculated substrate temperature profiles, the population induced by thermal electrons can be estimated (Fig. 8). Coupling to nascent electrons will occur only for the duration of the visible pulse with decay of the effect again governed by the T_1 time. The time scale for the different direct interactions between the CO stretch motion and the substrate electrons is limited by the decay time for T_e and adsorbate relaxation T_1 time. Signatures in the CO stretch spectra such as line broadening due to electronic dephasing or population induced decreases of absorption strength and spectral shifts, should therefore also appear and decay on these time scales.

5. Experimental Techniques

5.1. *Basic Plan of Experiments*

The experiment incorporates ultrafast visible, and tunable IR pulses with ultrahigh vacuum (UHV) technologies. Regarding the laser aspect of the experiment it is necessary to generate short ≤ 1 ps visible pulses and a narrow band, continuously tunable, infrared source. For our experiment, different frequency generation involving two visible pulsed lasers, one tunable, was used to produce the quasi-CW IR source. The resulting IR pulses possess peak powers of ~ 1 kW facilitating an up-conversion detection scheme which would not be feasible using a true CW IR source. The pulse duration necessary to separate electronic and surface temperatures varies from metal to metal according to the physical parameters discussed in Sec. 3. For platinum which has a relatively fast electron–phonon equilibration time, a 300 fs pulse will create a temperature difference ratio of four between the electrons and the phonons. In this section, the laser system will be described and the UHV diagnostics and sample conditions will be reviewed.

5.2. *Laser System*

A schematic of the apparatus is shown in Fig. 9. At the heart of the laser system[14,21,23] is a mode-locked Nd:YLF master oscillator, which delivers pulses of 70 ps in duration at a 76 MHz repetition rate. These pulses are frequency doubled in a heated LBO crystal yielding 1.8 W of the 527 nm radiation. The up-converted light is used to synchronously pump two dye lasers, and 500 mW of the remaining fundamental radiation (i.e. 1.053 μm) seeds a Nd:YLF regenerative amplifier. One of the dye lasers with a hybrid mode-locked dispersion compensated design uses Rhodamine 590 as a gain medium and a 2/3 mixed solution of DODCI/DQOCI as a saturable absorber to generate 200 fs pulses at 590 nm. The other dye laser operates with a single jet, a 3-plate birefringent filter and an intercavity etalon in the cavity, producing narrow band (1 cm^{-1}), tunable (580–610 nm), 30 ps pulses. The 1 kHz doubled output of the regenerative amplifier (1 mJ, 60 ps, 527 nm) provides pump energy for a series of dye amplifiers. The dye amplification cells, arranged in two stage pairs, with pump energy ratios of 20%–80% for the first and second stages respectively, use Rhodamine 610 with water as a gain medium and are pumped collinearly. The femtosecond

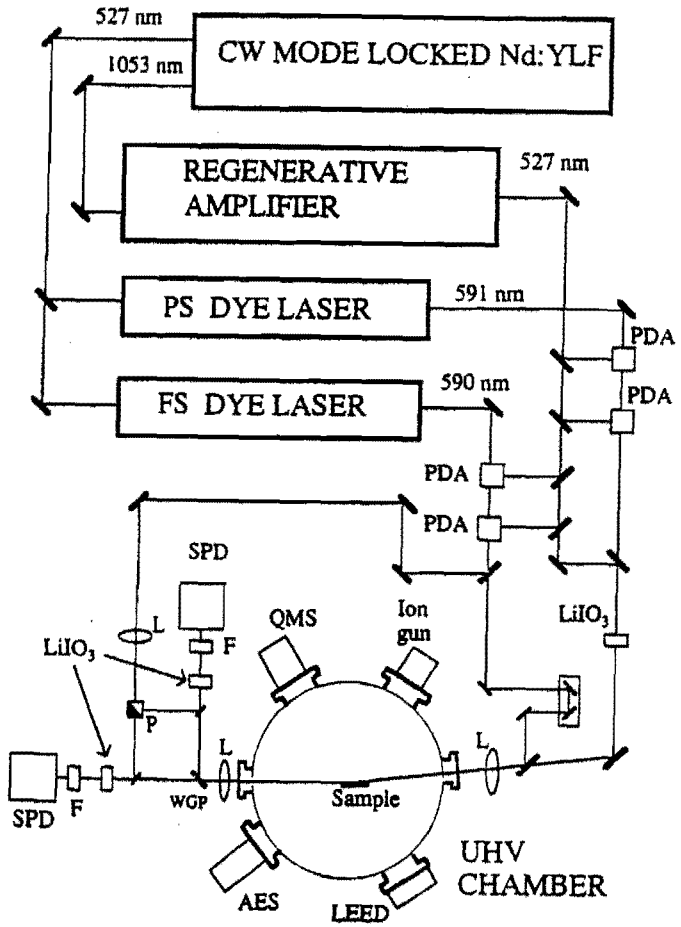

Fig. 9. Schematic of the apparatus. FS DYE LASER, synchronously pumped hybrid mode-locked dye laser (pulses ~ 200 fs in duration); PS DYE LASER, synchronously pumped dye laser (pulses ~ 30 ps); PDA, pulsed dye amplifier cells; F, spectral filter; SPD, silicon photodiode; L, lens; WGP, wire grid polarizer; P, polarizer; LEED, low energy electron diffraction; AES, Auger electron spectrometer; QMS, quadrupole mass spectrometer.

pulses are amplified by a set of dye cells with 500 μJ total pump power, using a copropagating first stage and counter-propagating second stage.

The picosecond pulses are amplified by the other set of amplifiers with 100 μJ total pump power, and both stages copropagating.

The resulting femtosecond pulses (4 μJ, 300 fs) are then split into pump and gating pulses, while the amplified picosecond pulses (3 μJ, 30 ps), are down-converted by difference-frequency generation in a 1 cm $LiIO_3$ crystal with 200uJ of the remaining doubled regenerative amplifier output. Tunable (1800–2100 cm^{-1}) quasi-CW, 10 nJ infrared pulses with a spectral full width of 1 cm^{-1} are produced.

The pump visible pulses and probe IR pulses were made collinear and using a 2f focusing relay introduced into a UHV chamber containing the Cu(111) crystal sample. The visible pump pulses are *p*-polarized, and the IR beam polarization was adjusted to be 70% *p*-polarized and 30% *s*-polarized. For low fluence experiments, at an incident angle of 85°, beam waists of 90 μm and 176 μm for visible and IR respectively, were used to generate a fluence absorbed of $F_{abs} = 0.09$ mJ/cm^2. The higher fluence experiments were accomplished at lower incidence angle (78°) with both beam waists ~ 180 μm. The resulting absorbed fluence ranged from 0.1 to 0.5 mJ/cm^2.

Time-resolved *detection* is accomplished by different frequency mixing of the IR beam reflected off the sample with the optically delayed visible gating pulses in $LiIO_3$ crystals. A wire grid polarizer is used to separate the *p*-polarized and *s*-polarized components of the IR beam. Subsequent up-conversion of these components in separate $LiIO_3$ crystals produces pairs of visible pulses (~ 675 nm) which are detected by two sets of matched photodiodes, amplifiers, and spectral filters. Since the adsorbed CO stretch vibrations only absorb energy from the *p*-polarized IR field, the *s*-polarized reflected beam provides a useful reference signal for normalization on every laser shot. Timing and overlap of the pulses are independently checked by examination of the transient reflectivity signal from a silicon wafer located underneath the Cu on the same sample manipulator. Finally, gated amplifiers are employed to acquire and ratio of *p*- and *s*-polarized transient reflectivity signals on a shot-by-shot basis.

5.3. *Vacuum System (Including Details About Desorption)*

The UHV chamber that houses the Cu(111) crystal sample utilizes a dual level chamber design.[21] The upper level contains an ion gun and basic surface diagnostics including LEED, AUGER, and quadrupole mass

spectrometry. The bottom level consists of a ring of view ports spaced by $\sim 30°$, some of which are CaF_2, for carrying out optical measurements with various incident angle geometries. Besides laser spectroscopy, the optical level is also used for reflection absorption infrared spectroscopy using a FTIR spectrometer.

A clean ordered Cu(111) surface is obtained by cycles of sputtering at 450 C and flash anneal to 600 C. The level of carbon, the major surface contaminant, as determined by Auger, is kept at less than 3% of a monolayer. Be dosing with 3L of CO at 95 K, and annealing to 125 K, subsequent cooling to 95 K produces an ordered overlayer with a $\left(\sqrt{3} \times \sqrt{3}\right) R30°$ pattern as confirmed by both LEED and FTIR linewidth measurements.

Important to the study of desorption is the threshold level of substrate excitation above which the desorption process occurs. We have determined this level using both SHG and IR absorption as time-resolved coverage sensitive probes. SHG from the Cu(111) surface provides information about the CO coverage (Fig. 10). Prybyla *et al.* were able to monitor desorption induced by 100 fsec 640 nm pulses using an SHG probe.[5] Although our observed SHG was not a linear function of coverage as in Ref. 5 (presumably due to the difference in laser frequency), we were able to place limits

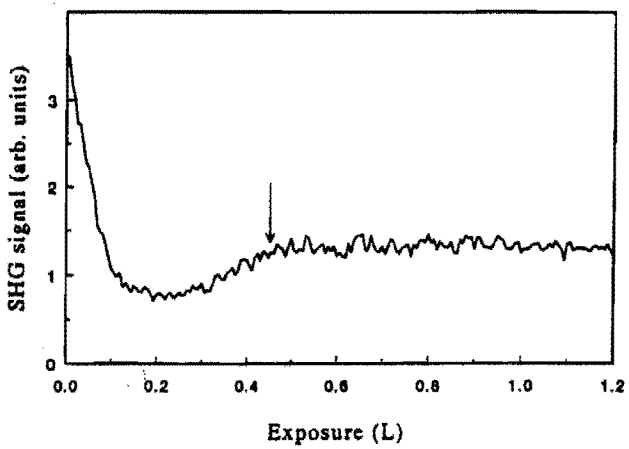

Fig. 10. Variation of surface SHG signal (at 295 nm) from a Cu(111) surface as a function of CO coverage (1 L = 1×10^{-6} Torr s). The arrow designates the exposure for the $\left(\sqrt{3} \times \sqrt{3}\right) R30°$ ordered overlayer where the transient heating measurements were performed.

on the desorption threshold. With a $\left(\sqrt{3} \times \sqrt{3}\right) R30°$ CO adlayer using the 590 nm visible pulse both as pump and SHG probe, we increased the fluence absorbed looking for deviations from the expected $I(2\omega) = \alpha I^2(\omega)$ dependence. At fluence levels which cause the molecules to desorb, the SHG signal changes in the direction of the undosed value. An upper limit of 2.5 mJ/cm^2 adsorbed fluence for the desorption threshold can be established from these measurements. Differential reflectivity also provides information about CO coverage. By observing where the signal strength decreases with an increase in fluence, a lower limit of 0.5 mJ/cm^2 absorbed fluence, for the desorption threshold can be placed. Combining the transient IR probe results and the SHG results suggest that the threshold lies between 0.5 mJ/cm^2 $< F_{abs} <$ 2.5 mJ/cm^2.

6. Results and Discussion

In the general description of the infrared response developed in Sec. 2, we found that the physics of the relaxation phenomena is contained in the time variation of the complex frequency $\Delta S(t, t_p)$ and the population $n_0(t)$. As mentioned above, at very high fluences there may be population in $v = 1$ which will complicate matters, but the experiments and calculations show this is minimal as discussed later. In principle, any theoretical model explicitly relating substrate evolution to the complex frequency and population can be tested. *A priori* there exist many possible effects. In this section, we will use the analysis developed in Sec. 2, along with experimental data to discuss possible substrate–adsorbate interactions outlines in Sec. 4.

The data of Fig. 11 depicts the general features of our differential reflectivity measurements as a function of probe IR frequency. Taken at a fixed time delay of 3.5 ps between the pump and the gate pulses, the data is characteristic of a shifting Lorentzian absorption. Note that the shift is a fraction of the linewidth, and since the feature is roughly symmetric we anticipate that the linewidth and integrated absorption remain roughly constant. Hence, explanations which involve a loss of adsorbers by mechanisms such as diffusion, desorption or dissociation appear unlikely from the outset. Frequency scans taken at longer relative delay times show that the feature remains basically the same with a decreased amplitude. Our conclusions are similar to those obtained in the other visible pump/IR probe experiments by Germer *et al.* for CO on Pt(111) [Ref. 15] and Cu(100) [Ref. 16].

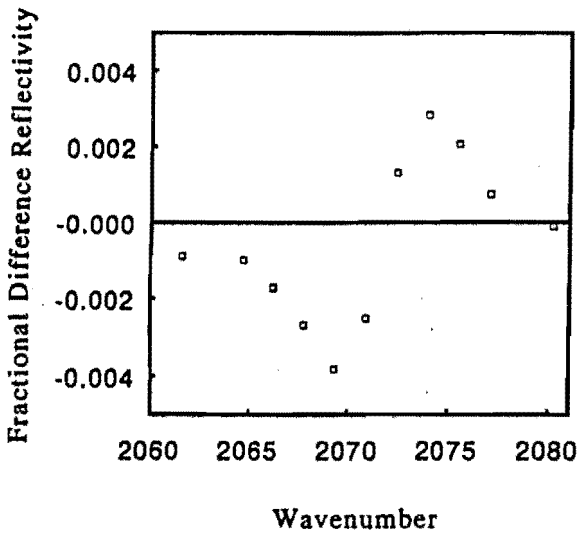

Fig. 11. Difference reflectivity signal as a function of the IR probe frequency. The data were taken at a time delay of 3.5 ps with $F_{abs} = 0.4$ mJ/cm^2. The derivative shape is characteristic of a shifted Lorentzian that often arises in temperature dependent studies of vibrational line-shapes. Similar spectra were obtained at $F_{abs} = 0.087$ mJ/cm^2.

6.1. *Low Fluence:* $F_{abs} = 0.09$ *mJ/cm*^{2}

The mechanisms brought out in Sec. 4, provide testable models for the observed dynamics. In Fig. 12 we exhibit measured transient reflectivity with the probe laser tuned off resonance by 1.5 cm^{-1} to the higher energy side of the 2073.5 cm^{-1} resonance. We see that the signal rises, peaks at $\sim$ 3 ps, and then exponentially decays with a characteristic time of $\sim$ 3 ps returning to a plateau $\sim$ 40% the peak value. These features clearly rule out direct excitation of the CO stretch by either nascent or thermal electrons. Direct excitation by nascent electrons would occur during the 300 fs visible pulse duration. The new population would subsequently decay with the CO stretch T_1 time of $\sim$ 1–2 ps. Neither the signal growth kinetics, the 3 ps decay nor the plateau can be accounted for with such a scenario. The magnitude of the signal due to thermal population of the CO stretch can be estimated with Eq. (35). At the current fluence levels,

the $v = 1$ C-O mode obtains a peak population of $1x10^{-4}$. Multiplying this change in population times the 5% static absorption places an upper limit on the signal strength at $5x10^{-6}$, about $1x10^{-3}$ smaller than the signal we observe. Instantaneous dephasing processes involving substrate electron hole pairs would cause line broadening. As evident in the model for an impulsive perturbation [Eq. (14) and Fig. 4] an instantaneous line broadening would grow in with the new T_2 dephasing time which, by assumption, would be extremely short. The smoothness of the rising edge data in Fig. 12(b) rules out the existence of any fast components in the new absorption at current signal to noise levels.

One simple model remains, whereby the CO internal stretch is anharmonically coupled to a lower frequency surface adsorbate mode, as described in Sec. 4.2. We have performed static FTIR measurements as a function of substrate temperature to confirm that this model adequately

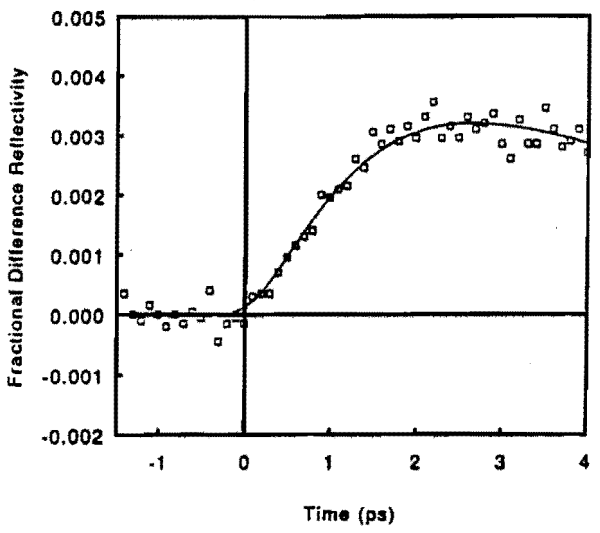

(a)

Fig. 12. (a) Rise of the fractional difference reflectivity signal ($\Delta R/R$) at 2075 cm^{-1} as a function of time after the visible heating pulse. The solid line is the best-fit to the data using the anharmonic coupling model discussed in the text with our best estimates for the low frequency reservoir coupling rates, $\gamma_e = 167$ GHz and $\gamma_l = 145$ GHz. (b) Time evolution of the fractional difference reflectivity signal over full time range. The solid line is the same fit as in (a).

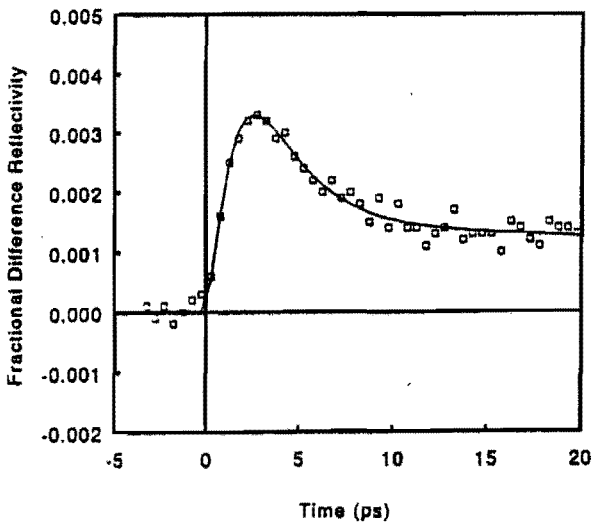

(b)

Fig. 12. (*Continued*)

describes the temperature-dependent complex frequency shift over a limited range of temperatures 95° K – 125° K (Fig. 13(a)). For example, within this temperature range the measured CO stretch lineshift varies linearly according to $\omega_{10} = [2078.4 - 0.052 * T]$ cm^{-1}. This variation indicates we are in the high temperature limit of the exchange theory. That is, the low frequency mode has an energy level separation considerably less than the thermal energy at 100 K. Since the frequencies of the frustrated rotation ($\omega_{FR} \sim 281$ cm^{-1}) and the Cu-CO stretch ($\omega_{\text{Cu-CO}} \sim 330$ cm^{-1}) are too high to account for the FTIR data, the frustrated translation with a theoretically expected frequency < 100 cm^{-1} is proposed to be the dephasing mode. This assignment is also supported by studies of atop bound CO on Pt(111) [Refs. 50, 51], and Cu(100) [Ref. 15], Ru(100) [Ref. 52]. In all these examples the frustrated translation dephases and shifts the frequency of the stretch mode. Separate line broadening measurements were consistent with the lineshift measurements. Equation [13(b)] predicts a quadratic high temperature limit for the dephasing rate (linewidth) of the CO-stretch transition and we modeled $\gamma(T)$ accordingly obtaining a best quadratic fit

$\gamma(T) = (4.85 + 0.000065T^2)$ cm^{-1}.

We have analyzed the data of Fig. 12 using the anharmonic coupling model. The temperature variation of the low frequency oscillator (Fig. 5), was determined using Eq. (37), and the complex frequency of the CO stretch mode was obtained from the parameters derived from FTIR data. Relating the features of the experimental data to the substrate tempera tures, the phonon temperature profile seems an unlikely candidate as the sole driving force of the adsorbate response. If the electronic temperature

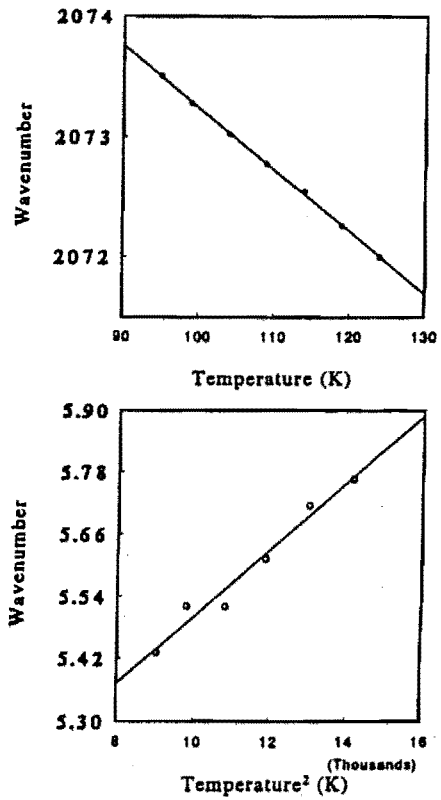

Fig. 13. Temperature dependence of the CO stretch complex frequency, obtained from Lorentzian fits to FTIR spectra. The solid lines are best-fits to the data (circles) using the stochastic Brownian oscillator model described in the text: (a) center frequency $\omega_{10}(T)$, and (b) linewidth $\gamma_{10}(T^2)$.

is responsible for the peak feature in the adsorbate response then something delays the peak by 2 ps. This delay can again be understood by using the model of an impulsive perturbation discussed in Sec. 2.3. From Eq. (14) and Fig. 4(b), one can see that for an instantaneous shift in frequency, a new absorption grows in with the inverse of the new linewidth. In the experiment, the temporal profile of the frequency shift, following T_{osc}, must be convoluted with time variant complex frequency to obtain the measured optical response [see Eq. (12)]. For small frequency shifts, and small detunings the new signal will grow in with a response time of $\gamma_0 \sim 2.2$ ps and hence the signal measured peaks roughly 2 ps after the peak adsorbate temperature.

Fits of the data using Eq. (12) reveal that couplings to both electrons and phonons are present. Our best estimates[a] for the low frequency reservoir coupling rates, $\gamma_e = 167(24)$ GHz and $\gamma_l = 145(52)$ GHz, give the solid lines shown in Fig. 12, and give the adsorbate temperature variation shown in Fig. 5 (see solid line). The effects of finite laser spot sizes[b], and finite pulse durations[c] were measurable, and were explicitly included in these fits. We note that γ_l is not as well determined as γ_e. The error in γ_l was obtained using γ_e and its error, along with the measured exponential decay rate (and its error) for data after 4 ps. The signal in this time regime is expected to decay exponentially at a rate of approximately the sum of γ_e and γ_l.

As noted in Sec. 3, the expected response is sensitive to the assumed electron–phonon coupling constant g. In fact we have found that our measurements can only be fit when g is in the range $0.5\text{–}2.0 \times 10^{17}$ W/m^{3}K. Therefore we use the value of 1.0×10^{17} W/m^{3}K reported by Ref. 28. The measurements clearly reveal that a low frequency vibrational mode, presumably the frustrated translational mode, couples to both electron and phonon bulk temperature reservoirs on a time scale of 5 ps. These times are of the same order of magnitude as recent temperature-dependent theoretical predictions for electron and phonon coupling to the frustrated translational mode of CO on Cu(100) [Ref. 53] and to the experimental results for CO on Cu(100) [Ref. 16].

[a]Current investigations of the wavelength and fluence dependence of the coupling rates γ_e, and γ_l, indicate that the quoted values may require slight revision. This work will be published soon.

[b]For our spot sizes, the peak fluence is 4 × the average fluence. To account for this, we convoluted Eq. (12) with the appropriate gaussian weighted distribution of fluences.

[c]Equation (12) was convoluted with a 300 fs gaussian pulse.

Up to now the analysis has presumed a single CO molecule on an infinite copper surface. The actual adsorbate structure is a $(\sqrt{3} \times \sqrt{3})\,R30°$ ordered overlayer. There is therefore a band of levels characterized by exciton wave vectors $\{\mathbf{k}\}$. The bandwidth is determined by interactions between the dipoles created by oscillations of the CO bond. The infrared probe absorption involves only the levels at $\mathbf{k} \sim 0$. Such a pin cushion array of dipoles is well-known to yield a negative coupling constant for each pair of molecules and hence an inverted band, with $\mathbf{k} = 0$ at the top. This picture is consistent with IRRAS studies of isotopic mixtures of CO on Cu(111) [Ref. 54]. The measured nearest neighbor coupling energy of 40 cm^{-1} corresponds to a characteristic period of 415 fs for the damped oscillatory motion of the probability that the vibrational excitation will remain on any given molecule. Since the relaxation time of the mode is 1.2 ps it may be safely assumed that the vibrational excitations are not completely localized by the coupling to the surface. However, when the excitation does jump to another site during the relaxation time the argument used here to describe the spectral changes would be unaffected if the sites were identical. The motion corresponding to the frustrated translation does not generate a dipole perpendicular to the surface, thus the bandwidth in this case is expected to be small and these excitations will be immobilized on the time scales of their coupling to the bath.

Before considering the system response to higher levels of excitation it is worthwhile to review the limitations of our model. The model assumes temperature-independent coupling rates, and essentially extrapolates static FTIR data obtained at $\sim 100°$ K to temperatures (albeit transient temperatures) in considerable excess of these values. The model treats the frustrated translation as an ideal harmonic oscillator, ignoring anharmonicities that may be important at high temperatures. The possible effects of other low lying vibrational modes, particularly of surface waves that may couple to or be involved in the frustrated translation motion are not incorporated and need to be considered in more detail. On the other hand, the data clearly indicate that the model is a good starting point by which to understand these phenomena at low levels of substrate excitation.

6.2. *Higher Fluence: Temperature-Dependent Relaxation*

At sufficiently high levels of substrate excitation, the severe electron temperatures induce the CO molecules to desorb. A model involving desorption

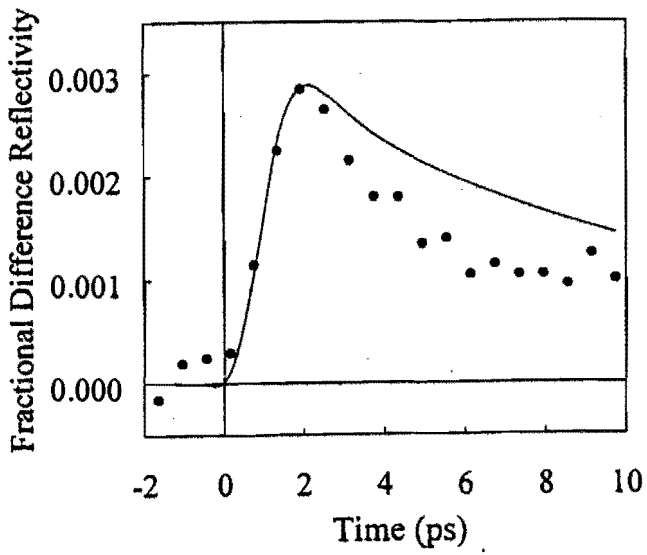

Fig. 14. Differential reflectivity on the high frequency side of the CO stretch resonance for $F_{abs} = 0.75$ mJ/cm^2. The dashed line is the model prediction using the lower fluence coupling rates.

induced by multiple electronic transitions (DIMET) has been developed to explain the highly nonlinear yields which characterize femtosecond desorption processes experimentally observed for CO on Cu(111) [Ref. 5], NO on Pd(111) [Refs. 2, 3], O_2 on Pt(111) [Ref. 55] and O_2 on Pd(111) [Ref. 8]. In addition, studies of the vibrational states of desorbed NO molecules reveal that the NO stretch is vibrationally excited upon leaving the surface.[4] Generally, as adsorbed molecules acquire energies nearly sufficient for desorption, anharmonic couplings between the different adsorbate modes play an increased role in energy transfer processes. Approximations of the adsorbate vibrations as uncoupled oscillators become less valid and low excitation coupling rates and models may not be applicable.

The data of Fig. 14 depicts the time evolution of the differential reflectivity on the high frequency side of the CO stretch vibration for $F_{abs} \sim 0.75$ mJ/cm^2. The dashed line shows the preliminary prediction of the model using the low fluence coupling rates. As can be seen, the decay of the data is considerably faster ($\sim 2\times$) than the model prediction and the

plateau is lower at about 20% the peak value. A comparison of these results with recent calculations of Tully and coworkers[53] is worthwhile. Using molecular dynamics calculations which incorporate electronic friction they predict temperature-dependent coupling rates for the CO/Cu(100) system. They find that the FR coupling to the electron bath is much faster than that of the FT at low temperature: As the temperature is raised, the two rates become more comparable, although the coupling to the FR remains larger at all temperatures. For example, the products of the electron coupling rate constants and the Boltzman factors for the FR and FT remain within a factor of three over the whole temperature range of the calculation, 10–450 K. That calculation also predicts that the effective electron coupling to the FT, as measured by the foregoing product will increase almost linearly with T whereas the FR coupling is closer to quadratic. This suggests that at still higher T the FR might be more important than the FT. However, if the FR and FT were anharmonically coupled to the CO stretch to any reasonable extent, then exchange theory used with the calculated rate constants would predict a nonlinear contribution to the shift vs T curve by the FR. For the temperature range studied the observed shift was quite linear, as shown in Fig. 13, indicating that the coupled mode is in the high T limit. Another important prediction of this calculation is that the FT mode is very anharmonic, of course in our analysis it was assumed to be harmonic.

A more serious caveat associated with the comparison of our results to these calculations is that they refer to situations where the entire system is in equilibrium, whereas our results are produced in a situation where the adsorbate modes, the electrons, and the phonons are at *different* temperatures. In order to make a comparison between theory and experiment one must identify what combination of these temperatures determine the coupling rates. For example, the increased coupling that appears to occur when the fluence is raised may arise from changes in the bath, and not from changes in the adsorbate nuclear configuration. However if this was the case, the latter stages of the relaxation, after the substrate had cooled rapidly (and nonexponentially!) to its low fluence temperature maximum, would be expected to be the same for all fluences. This is not what is observed. It seems unlikely that the small increases in the quasi-equilibrated bath temperature (i.e. after ca. 2 ps but before conventional diffusion equilibrates the surface and the bulk) resulting from the increases in fluence could be the cause of the observed effects.

Alternatively, the rates may be determined by the different adsorbate-like mode temperatures. After the peak of the signal, the bath is equilibrated at some slightly elevated temperature ($\delta T_e \sim \delta T_l \sim +5$ K for $F_{abs} = 0.09$ mJ/cm^2) but the adsorbate FT is hot ($\delta T_{FT} \sim +25$ K) as shown in Fig. 5. At higher fluence the FT temperature at the signal peak may reach as high as 200 K above the substrate temperature. The other adsorbate modes will similarly have elevated temperatures causing the adsorbate structure to be much more severly shifted from equilibrium at higher fluences. It is possible that this could produce a sufficient alteration of the electronic structure so that the coupling to the substrate would be substantially increased. To make a quantitative evaluations of such effects more detailed knowledge about the adsorbate modes are needed. Systematic studies of the excitation-dependence of the low frequency mode coupling rates, however should provide a clearer picture of the complex development of vibrational excitation in CO as it approaches the desorption threshold.

7. Conclusion

In this contribution we have discussed a novel way to measure the coupling rate of the frustrated translation vibration to the substrate electrons and phonons. The three low frequency adsorbate-like modes, are at frequencies as yet not amenable to direct IR time-resolved spectroscopy. However, their couplings to the substrate are of much interest, particularly because they are the modes which, when sufficiently excited, lead to desorption. The CO stretch mode, with $\lambda \sim 5$ μm, is the only vibration to be directly monitored by ultrafast IR spectroscopy this far. The experimental method we have described, exploits the frequency shift of the stretch vibration induced by the frustrated translation mode. By monitoring the temperature of the frustrated translation, via the stretch frequency shift, ultrafast measurements of the relaxation of a sub 100 cm^{-1} vibration were obtained. Applications of this technique may have some utility in studies of other processes which shift adsorbate frequencies. A variety of other surface properties are known to shift the vibrational frequency of an adsorbate, including; coverage, the presence of coadsorbed species, binding sites and surface reconstructions to cite a few examples. Combining the novel environment created by femtosecond visible excitation of surfaces with the detailed mode specific descriptions of IR spectroscopy, much can be learned about ultrafast surface photoprocesses.

Acknowledgments

It is a pleasure to acknowledge useful conversations with Charles Kane, Gene Mele, Jeff Owrutsky, and Klaas Wynne. We also thank John Vohs and Bill Petrie for their work in obtaining the FTIR measurements. This work has been supported by the NSF MRL program through Grant # DMR-9120668. AGY acknowledges partial support from the NSF through the PYI Program, and from the Alfred P. Sloan Foundation. RMH acknowledges partial support through grants from the NIH and the NSF.

Appendix A

For a Hamiltonian involving a time-dependent stark shift we integrate the following Liouville equation,

$$\dot{\rho}_{01} = \frac{i}{\hbar}[p, H]_{01} - \Gamma_{01}(t)\rho_{01}\,. \tag{47}$$

The Hamiltonian is of the form;

$$H = \begin{pmatrix} E_0 & 0 \\ 0 & E_1 \end{pmatrix} + \begin{pmatrix} S_{00}(t) & 0 \\ 0 & S_{11}(t) \end{pmatrix} + \begin{pmatrix} 0 & V(t) \\ V(t) & 0 \end{pmatrix}, \tag{48}$$

where $V(t) = -\mu_{01}\mathcal{E}(t)\cos(\omega_L t)$, and $S_{ii}(t)$ is the time-dependent stark shift of the ith state. Writing out the commutator explicitly, Eq. (47) can be expressed,

$$\dot{\rho}_{01} + a(t)\rho_{01} = \frac{i}{\hbar}\Delta\rho V(t)\,, \tag{49}$$

where $a(t) = i\{\omega_{01} + \Delta S_{01}(t)\} + \Gamma(t)$, $\Delta S_{01}(t) = (1/\hbar)\{S_{00}(t) - S_{11}(t)\}$, and $\Delta\rho = \rho_{00} - \rho_{11}$. The response of the system to a driving field can be realized by multiplying Eq. (49) by

$$u(t) = u(t_0)e^{\int_{t_0}^{t} a(\tau)d\tau}\,, \tag{50}$$

and noting that

$$u(t)\frac{d\rho_{01}}{dt} + u(t)a(t)\rho_{01} = \frac{d}{dt}[u(t)\rho_{01}]\,. \tag{51}$$

For our purposes, the small signal approximation is valid and we can use $\Delta\rho(t) = n_0$. It is then straight forward to obtain

$$\rho_{01}(t) = \rho_{01}\frac{u(t_0)}{u(t)} + \frac{in_0}{\hbar}\int_{t_0}^{t} dt_1 \frac{u(t_1)}{u(t)}V(t_1)\,. \tag{52}$$

By taking $t_0 \rightarrow -\infty$ the first term goes to zero. Putting in explicit forms of $u(t)$ and $V(t)$ and taking the rotating wave approximation, we arrive at

$$e^{-i\omega_L t}\rho_{01}(t) = -\frac{i\mu_{01}n_0}{\hbar}\int_{-\infty}^{t} dt_1 \mathcal{E}(t_1)e^{-\int_{t_1}^{t}\Omega(\tau)d\tau}, \qquad (53)$$

where $\Omega_{01}(t) = i(\omega_L + \omega_{01} + \Delta S_{01}(t)) + \Gamma(t)$.

For processes (such as desorption) which deplete n_0, without creating a new coherence at ω_L, $\rho_{01}(t)$ can be described by Eq. (9) which is Eq. (53) with a time-dependent instantaneous population $n_0(t)$. In general, the transferred coherence should also be considered.[43]

References

1. R. R. Cavanagh, D. S. King, J. C. Stephenson, and T. F. Heinz, *J. Phys. Chem.* **97**, 786 (1993).
2. J. A. Prybyla, T. F. Heinz, J. A. Misewich, M. M. T. Loy, and J. H. Glowina, *Phys. Rev. Lett.* **64**, 1537 (1990).
3. F. Budde, T. F. Heinz, M. M. T. Loy, J. A. Misewich, F. deRougemont, and H. Zacharias, *Phys. Rev. Lett.* **66**, 3024 (1991).
4. F. Budde, T. F. Heinz, A. Kalamarides, M. M. T. Loy, and J. A. Misewich, *Surf. Sci.* **283**, 143 (1993).
5. J. Prybyla, H. Tom, and G. Aumiller, *Phys. Rev. Lett.* **68**, 503 (1992).
6. F. J. Kao, D. G. Bush, D. G. Dacosta, and W. Ho, *Phys. Rev. Lett.* **70**, 4098 (1993).
7. F. J. Kao, D. G. Bush, D. Cohen, D. G. Dacosta, and W. Ho, *Phys. Rev. Lett.* **71**, 2094 (1993).
8. J. A. Misewich, A. Kalamarides, T. F. Heinz, U. Hofer, and M. M. T. Loy, *J. Chem. Phys.* **100**, 736 (1994).
9. J. D. Beckerle, M. P. Casassa, R. R. Cavanagh, E. J. Heilweil, and J. C. Stephenson, *Phys. Rev. Lett.* **64**, 2090 (1990); J. D. Beckerle, M. P. Casassa, R. R. Cavanagh, E. J. Heilweil, and J. C. Stephenson, *J. Electron. Spectrosc.* **54/55**, 17 (1990).
10. J. D. Beckerle, R. R. Cavanagh, M. P. Casassa, E. J. Heilweil, and J. C. Stephenson, *J. Chem. Phys.* **95**, 5403 (1991); R. R. Cavanagh, J. D. Beckerle, M. P. Casassa, E. J. Heilweil, and J. C. Stephenson, *Surf. Sci.* **269/270**, 113 (1992).
11. P. Guyot-Sionnest, P. Dumas, Y. J. Chabal, and G. S. Higashi, *Phys. Rev. Lett.* **64**, 2156 (1990); P. Guyot-Sionnest, *J. Electron. Spectrosc.* **64/65**, 1 (1993).
12. A. L. Harris, L. Rothberg, L. H. Dubois, and L. Dhar, *Phys. Rev. Lett.* **64**, 2086 (1990).
13. A. L. Harris, N. J. Levinos, L. Rothberg, L. H. Dubois, L. Dhar, S. F. Shane, and M. J. Morin, *J. Electron. Spectrosc.* **54/55**, 5 (1990); A. L. Harris, L. Rothberg, L. Dhar, N. J. Levinos, and L. H. Dubois, *J. Chem. Phys.* **94**, 2438 (1991); M. Morin, N. J. Levinos, and A. L. Harris, *J. Chem. Phys.* **96**, 3950 (1992).
14. J. P. Culver, M. Li, L. G. Jahn, R. M. Hochstrasser, and A. G. Yodh, *Chem. Phys. Lett.* **214**, 431 (1993).
15. T. A. Germer, J. C. Stephenson, E. J. Heilweil, and R. R. Cavanagh, *J. Chem. Phys.* **98**, 9986 (1993).
16. T. A. Germer, J. C. Stephenson, E. J. Heilweil, and R. R. Cavanagh, *Phys. Rev. Lett.* **71**, 3327 (1993).
17. S. I. Anisimov, B. L. Kapeliovich, and T. L. Perel'man, *Zh. Eksp. Teor. Fiz.* **66**, 776 (1974).
18. R. G. Greenler, *J. Chem. Phys.* **44**, 310 (1966).
19. T. F. Heinz, Ph.D. Dissertation, University of California at Berkeley, 1982.
20. A. G. Yodh and H. W. K. Tom, *Phys. Rev.* **B45**, 14302 (1992).
21. J. C. Owrutsky, J. P. Culver, M. Li, Y. R. Kim, M. J. Sarisky, M. S. Yeganeh, A. G. Yodh, and R. M. Hochstrasser, *J. Chem. Phys.* **97**, 4421 (1992).
22. J. N. Moore, P. A. Hansen, and R. M. Hochstrasser, *Chem. Phys. Lett.* **138**, 110 (1987).
23. M. Li, J. C. Owrutsky, M. Sarisky, J. P. Culver, A. Yodh, and R. M. Hochstrasser, *J. Chem. Phys.* **98**, 5499 (1993).
24. P. A. Anfinrud, C. Han, and R. M. Hochstrasser, *Prc. Natl. Acad. Sci. USA* **86**, 8387 (1989).
25. J. C. Kimball, C. Y. Fong, and Y. R. Shen, *Phys. Rev.* **B23**, 4946 (1981).
26. P. Guyot-Sionnest, *Phys. Rev. Lett.* **67**, 2323 (1991).
27. G. L. Eesley, *Phys. Rev.* **B33**, 2144 (1986).
28. H. E. Elsayed-Ali, T. Norris, M. A. Pessot, and G. Mourou, *Phys. Rev. Lett.* **58**, 1212 (1987).
29. P. B. Corkum, F. Brunel, N. K. Sherman, and T. Srinivasan-Rao, *Phys. Rev. Lett.* **61**, 2886 (1988).
30. R. W. Schoenlein, W. Z. Lin, J. G. Fujimoto, and G. L. Eesley, *Phys. Rev. Lett.* **58**, 1680 (1987).
31. P. B. Allen, *Phys. Rev. Lett.* **59**, 1460 (1987).
32. S. D. Brorson *et al.*, *Phys. Rev. Lett.* **64**, 2172 (1990).
33. H. E. Elsayed-Ali, T. Juhasz, G. O. Smith, and W. E. Bron, *Phys. Rev.* **B43**, 4488 (1991).
34. W. W. Fann, R. Storz, H. W. K. Tom, and J. Bokor, *Phys. Rev. Lett.* **68**, 2834 (1992).
35. *American Institute of Physics Handbook*, 3rd Ed., ed. D. E. Gray (McGraw-Hill, New York, 1972).
36. M. Head-Gordon and J. C. Tully, *Phys. Rev.* **B46**, 1853 (1992).
37. E. J. Heilweil, R. R. Cavanagh, and J. C. Stephenson, *J. Chem. Phys.* **89**, 230 (1988).
38. C. B. Harris, R. M. Shelby, and P. A. Cornelius, *Phys. Rev. Lett.* **38**, 1415 (1977); R. M. Shelby, C. B. Harris, and P. Cornelius, *J. Chem. Phys.* **70**, 34

(1974); S. Marks, P. A. Cornelius, and C. B. Harris, *J. Chem. Phys.* **73**, 3069 (1980).
39. N. G. van Kampen, *Stochastic Processes in Physics and Chemistry* (North-Holland, New York, 1981).
40. B. N. J. Perrson and R. Ryberg, *Phys. Rev.* **B32**, 3586 (1985).
41. S. A. Adelman, *Adv. Chem. Phys.* **44**, 143 (1980).
42. *Selected Papers on Noise and Stochastic Processes*, ed. N. Wax (Dover, New York, 1954).
43. K. Wynne and R. M. Hochstrasser, submitted to *Chem. Phys.*.
44. R. Kubo and K. Tomita, *J. Phys. Soc. Jpn.* **9**, 888 (1954).
45. D. Menzel, *J. Vac. Sci. Technol.* **20**, 538 (1981).
46. V. Dose, *Surf. Sci.* **5**, 337 (1985).
47. B. Gumhalter, K. Wandelt, and P. Avouris, *Phys. Rev.* **B37**, 8048 (1988).
48. P. Avouris and R. E. Walkup, *Ann. Rev. Phys. Chem.* **40**, 173 (1989).
49. K. D. Tsuei and P. D. Johnson, *Phys. Rev.* **B45**, 13827 (1992).
50. A. M. Lahee, J. P. Toennies, and C. Woll, *Surf. Sci.* **177**, 371 (1986).
51. E. Schweizer, B. N. J. Persson, M. Tushaus, and A. M. Bradshaw, *Surf. Sci.* **213**, 49 (1989).
52. B. N. J. Persson, F. M. Hoffman, and R. Ryberg, *Phys. Rev.* **B34**, 2266 (1986).
53. J. C. Tully, M. Gomez, and M. Head-Gordon, *J. Vac. Sci. Technol.* **A11**, 1914 (1993).
54. B. N. J. Persson and A. Liebsch, *Surf. Sci.* **110**, 356 (1981).
55. F. J. Kao *et al.*, *Phys. Rev. Lett.* **71**, 2094 (1993).
56. P. Hollins and J. Pritchard, *Surf. Sci.* **89**, 486 (1979).
57. R. Raval *et al.*, *Surf. Sci.* **230**, 353 (1988).
58. C. J. Hirschmugl, G. P. Williams, F. M. Hoffmann, and Y. J. Chabal, *Phys. Rev. Lett.* **65**, 480 (1990).